Full Length Article

An insight into CO_2 sequestration and EGR in Longmaxi and Niutitang shale formations via experimental analysis

Chima Finnian Ukaomah [a,b], Mengdi Sun [a,b,*], Zhejun Pan [a], Mehdi Ostadhassan [a,c,d], Bo Liu [a], Yanran Xu [a], Agwom Istifanus Madaki [e], Happiness Ijeoma Umeobi [f,g], Mohammed Dahiru Aminu [h], Baolin Yang [b]

[a] Key Laboratory of Continental Shale Hydrocarbon Accumulation and Efficient Development, Ministry of Education, Northeast Petroleum University, Daqing 163318, China
[b] Key Laboratory of Tectonics and Petroleum Resources, Ministry of Education, China University of Geosciences, Wuhan 430074, China
[c] Institute of Geosciences, Marine and Land Geomechanics and Geotectonics, Christian Albrechts Universität, Kiel 24118, Germany
[d] Department of Geology, Ferdowsi University of Mashhad, Mashhad, Iran
[e] Department of Geology, University of Jos, P.M.B 2084, Jos, Plateau State, Nigeria
[f] Wuhan Institute of Rock and Soil Mechanics, Chinese Academy of Sciences
[g] Nnamdi Azikiwe University, Awka, Anambra State, Nigeria
[h] Federal Ministry of Environment, Mabushi, Abuja, Nigeria

ARTICLE INFO

ABSTRACT

In the global effort toward climate change mitigation, geologic storage of CO_2 in shale plays is becoming critical while it can improve production from these reservoirs. In this study, the gas storage capacity and CO_2 sequestration suitability of the Longmaxi and Niutitang shale gas reservoirs is investigated and compared via XRD analysis, programmed pyrolysis, low pressure N_2 and CO_2 adsorption, high pressure CH_4 adsorption, and MICP analysis. Results showed that clay and TOC controls on micropore heterogeneity and connectivity happens only within the Longmaxi Formation. Furthermore, both components play a role in the adsorbed quantities of gas in the formation which revealing a higher storage capacity in mesopore-macropores. This was verified by a positive correlation between adsorbed volume within the mesopore-macropore space. The Longmaxi Formation was also found to own better pore connectivity and PSD homogeneity of mesopore-macropores, indicating easier pathways for CO_2 movement channels within the pore network. Furthermore, the samples from the Longmaxi exhibited a positive relationship between adsorbed volume with the CO_2 breakthrough pressure and median pore diameter, alike between the mesopore-macropore volume and CO_2 breakthrough pressure. This means, the injected CO_2 will displace adsorbed methane within the mesopore-macropore and will be adsorbed and stored in such pores. Overall, superiority of the Longmaxi shale over the Niutitang for CO_2 storage and EGR would be significant for future operations in similar shale gas reservoirs in China and around the globe.

1. Introduction

Carbon capture, utilization, and storage (CCUS) describes an aggregate of technologies involved in the separation of carbon dioxide (CO_2) from industrial sources, transportation of the captured CO_2 to specific locations, and recycling or geological storage of the transported CO_2 [1]. The importance of CCUS to the global effort at combating against climate change is found in anthropogenic CO_2 emissions being a major enabler of global warming [2]. China accounting for 27.8% of the global CO_2 emissions [3], is using geological storage of CO_2 to reach 10% of total emission by 2030 [4]. This means, CCUS will play a critical role in China's ambition to achieve carbon neutrality before 2060 [5].

In this regard, CO_2 geological storage mimics the process of hydrocarbon trapping over millions of years. The captured CO_2 is compressed and injected into reservoir rocks in the subsurface sealed by impermeable layers, which then prevents upward CO_2 migration via various mechanisms [6], including capillary, adsorption, dissolution, and mineral trapping [7]. The suitability of hydraulically fractured shale reservoirs for CO_2 storage is due to the dominant adsorption trapping mechanism, owing to the presence of an already existing fracture
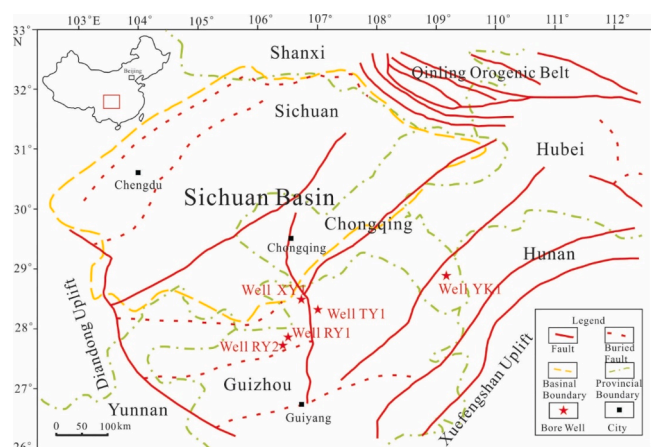
Fig. 1. Sichuan basin geologic map showing well locations (modified from Sun et al. [63]).

network. In such a case the injected CO_2 can simultaneously be used for enhanced gas recovery (EGR) operations which can significantly become cost effective [8,9].

Gas in shale is either stored as free molecules within fractures or in the adsorbed form in the organic matter which has a higher affinity for CO_2 than methane [10], and is mostly accessed via the inorganic matrix [11]. While the former ensures a displacement of adsorbed methane when CO_2 enhanced gas recovery is undertaken via CO_2 injection into hydraulically fractured shale reservoirs [12,13,65], the resulting impact of the recovery process on micro (<2 nm pore diameter), meso (2 nm – 50 nm pore diameter), and macro (>50 nm pore diameter) porous shale pore structure has necessitated several laboratory evaluations of shale interaction with CO_2.

This process can alter the total pore volume, pore size distribution (PSD), and dominant pore throat diameter which can be evaluated via laboratory techniques such as gas adsorption [14-16], and mercury injection capillary pressure (MICP) [17]. At the same time, these methods can provide us with the storage capacity of shale reservoirs, since this information is important for storage operations from different angles [18].

For instance, several studies have used an integration of gas

Table 1
Mineralogic and geochemical characteristics of the samples.

| Formation	Sample	Well	Depth (m)	Organic content and maturity		Whole rock minerals (*wt.%*)					
				TOC content (%)	R_o (%)	Clay	Quartz	Plagioclase	K-feldspar	Carbonate	Pyrite
Longmaxi	XY1-2	XY1	610	1.02	2.94	53	32	6	0	15	1
	XY1-3	XY1	621.5	1.09	2.67	28	20	5	1	44	2
	XY1-4	XY1	637	3.84	2.34	31	45	8	0	13	3
	XY1-7	XY1	643.5	4.88	2.21	18	26	3	0	50	3
	TY1-15	TY1	670.7	5.3	1.95	27	53	6	0	15	1
	TY1-18	TY1	674	3.86	2.45	16	61	7	0	12	3
Average				3.79	2.43	28.83	39.5	5.83	0.17	28.83	2.17
Standard Deviation				1.85	0.35	13.23	16.08	1.72	0.408	17.31	0.98
Niutitang	YK1-24	YK1	25.9	3.66	2.98	22	37	10	0	25	6
	YK1-37	YK1	36.98	5.69	3.12	26	54	5	0	10	5
	YK1-47	YK1	49.58	9.83	3.31	30	45	11	0	6	6
	RY2-13	RY2	919.1	12.5	3.01	9	81	3	0	3	4
	RY1-6	RY1	1310	3.51	3.23	45	37	9	0	4	5
	RY1-8	RY1	1330	5.95	3.89	29	47	10	0	6	8
Average				6.86	3.26	26.83	50.17	8	0	9	5.67
Standard Deviation				3.59	0.34	11.72	16.43	3.23	0	8.19	1.37
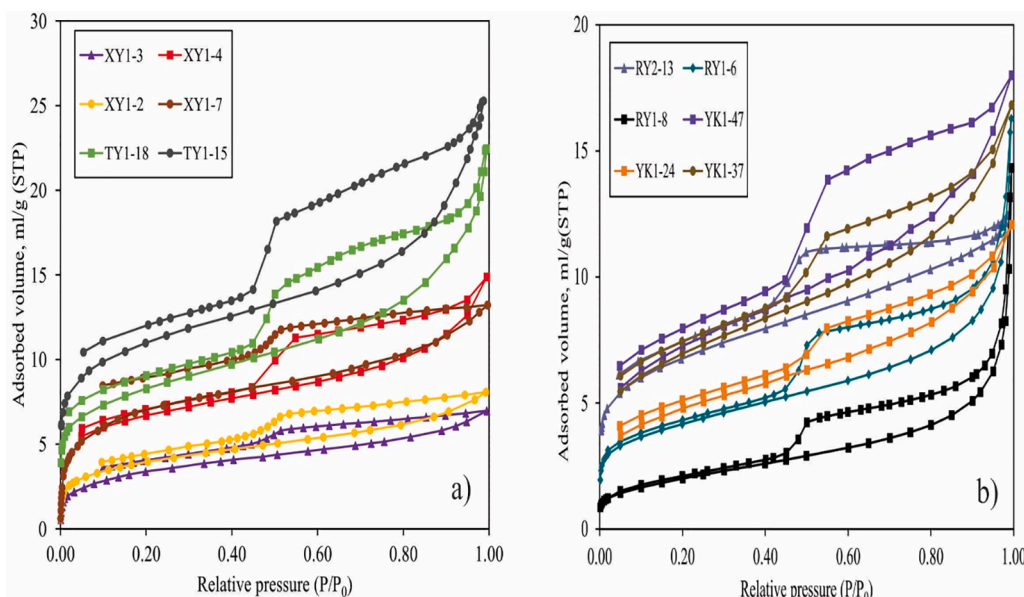
Fig. 2. Low pressure Nitrogen adsorption/desorption from (a) Longmaxi and (b) Niutitang samples.

Table 2
Low pressure CO_2 and N_2 adsorption analysis results.

Formation	Sample	Pore volume (ml/g)		Specific surface area (m^2/g) BET
		N_2 sorption (1.4 – 300 nm) DFT	CO_2 sorption (0.3 – 1.4 nm) DFT	N_2 sorption (1.4 – 300 nm) BET
Longmaxi	XY1-2	0.0083	0.001	14.20
	XY1-3	0.0073	0.004	12.55
	XY1-4	0.0108	0.005	22.82
	XY1-7	0.0112	0.004	24.65
	TY1-15	0.0290	0.010	39.20
	TY1-18	0.0310	0.019	29.37
Average		0.016	0.007	23.8
Standard Deviation		0.011	0.0065	9.89
Niutitang	YK1-24	0.0196	0.0030	16.39
	YK1-37	0.0260	0.0069	22.31
	YK1-47	0.0280	0.0086	25.96
	RY2-13	0.0178	0.0067	24.14
	RY1-6	0.0194	0.0030	14.72
	RY1-8	0.0160	0.0040	12.02
Average		0.021	0.0054	19.26
Standard Deviation		0.005	0.0024	5.64

adsorption, electron microscopy (FE-SEM), and MICP laboratory techniques to investigate pore structure and pore composition controls on gas adsorption in the Longmaxi [19-21], and Niutitang shales [22-24]. Furthermore, comparative experimental investigations of both formations undertaken via an integration of these techniques with high-pressure methane adsorption [25], have linked the difference in adsorbed gas capacity of both formations to variation in the volume of organic hosted pores. However, implications of this variation on CO_2 storage are yet to be evaluated for both formations.

In this study, methane, CO_2, and nitrogen adsorption, in conjunction with MICP are used to investigate the gas storage capacity and CO_2 sequestration suitability of the marine Longmaxi and Nuititang shale gas reservoirs. This study will enable us to find shale formations with the highest potential for CO_2 storage, and ultimately improve the accuracy of CO_2-EGR simulation models in shale gas reservoirs.

2. Geologic setting

The Upper Yangtze Platform of southern China encompasses Henan, most parts of Guizhou, eastern Sichuan, Chongqing, western Hubei and Hunan, and northern Yunan Provinces [26]. The platform was affected by the superimposition of multistage tectonic movements in different periods which resulted in the formation of faults and folds [27], with thick black shale sedimentary facies thickening from northwest to southeast as deposition changed from marine platform to open marine shelf [26,27]. This happened due to the global rise in sea levels during the early Cambrian period resulting in a transgressive marine epoch which favored deposition of carbonaceous and calcareous shale, carbonate, and siltstone [26]. Black shales extensively deposited on the Upper Yangtze Platform because of this transgression resulted in the deposition of the Lower Silurian Longmaxi shale and Lower Cambrian Niutitang shale.

The Lower Silurian marine Longmaxi is a shale gas reservoir, characterized by a high thermal maturity and total organic carbon, along with good porosity and fracturing potential [28,64]. The formation is characterised by total organic carbon (TOC) ranging from 0.50% to 25.73% [29], a gas field with proven reserves of 3200×10^8 cubic fit of gas with burial depth ranging from $1500 - 4500$ m [30], and gas generation that is due to sediment deposition in a tectonically stable, biogenic rich, low energy, and oxygen deficient deep water continental shelf [30].

The Lower Cambrian Niutitang Formation which comprises of black shales deposited within a deep-water continental shelf environment [24], are characterised by TOC ranging from 0.355 to 22.15% [29]. The regional geology of both the Niutiang and Longmaxi shale formation has been fully described in several studies [31,32], with studies using carbon isotope composition to note kerogen from both formations as marine oil prone organic matter formed in an anoxic environment [33]. However, in comparison to the Longmaxi Formation, studies have found the Niutitang Formation to have a higher brittleness due to deposition in a more restricted marine environment which makes it a perfect candidate for hydraulic fracturing [34]. In addition, unlike the Longmaxi shale, gas generation within the formation was inhibited by multi-stage tectonic deformation [35]. However, studies have noted favourable gas enrichment and accumulation conditions of $1.10 - 1.49$ m^3/t within the Niutitang shales, buried at 800 – 1600 m depths in northern Guizhou [36].
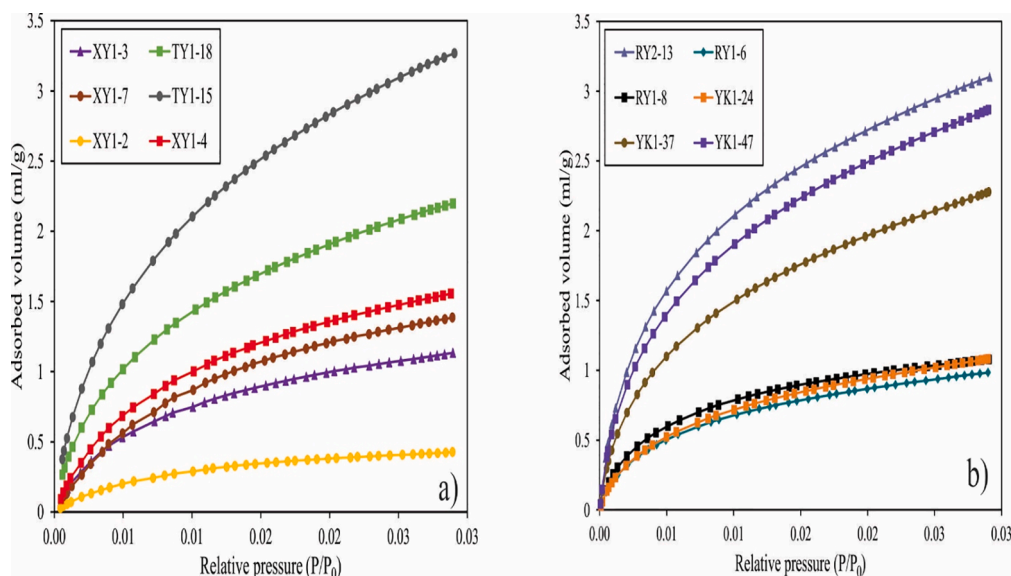
Fig. 3. Low pressure CO_2 isotherms obtained from (a) Longmaxi and (b) Niutitang samples.
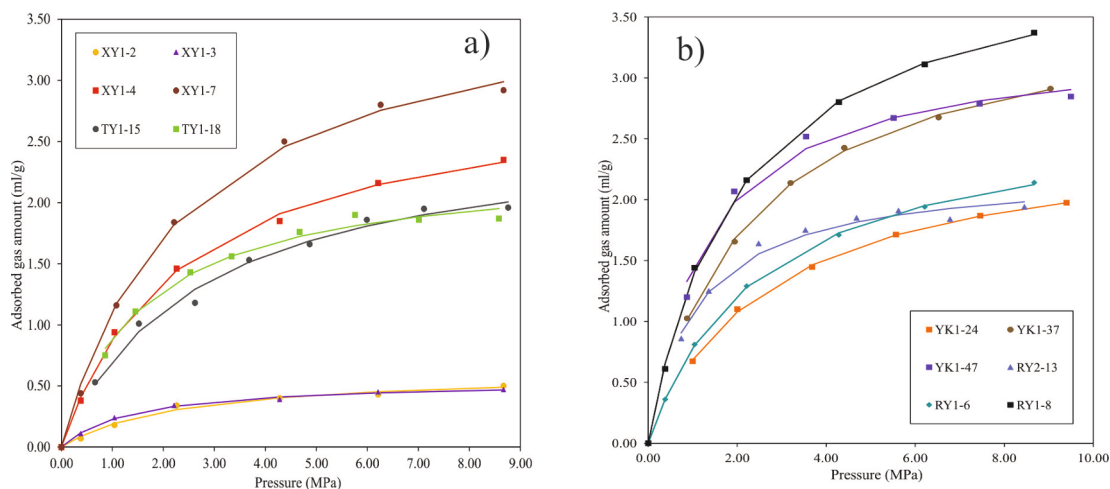
Fig. 4. Langmuir fitted methane sorption isotherms obtained from (a) Longmaxi and (b) Niutitang samples.

Table 3
Methane adsorption results obtained from the samples.

Longmaxi Shale			Niutitang Shale		
Sample	Langmuir maximum amount of adsorbed gas (ml/g)	Langmuir constant (1/MPa)	Sample	Langmuir maximum amount of adsorbed gas (ml/g)	Langmuir constant (1/MPa)
XY1-2	0.477	1.299	YK1-24	1.480	1.720
XY1-3	1.430	0.379	YK1-37	2.899	1.252
XY1-4	2.149	1.383	YK1-47	11.448	0.288
XY1-7	2.656	1.442	RY2-13	25.274	0.089
TY1-15	1.542	1.702	RY1-6	1.818	1.506
TY1-18	3.808	0.609	RY1-8	4.023	1.030

3. Sample collection and analyses

A total of twelve shale samples were obtained from 5 wells that were drilled through Longmaxi and Niutitang shales in the northeast of Guizhou and southeast of Chongqing deposition centres on the Upper Yangtze Platform (six samples for each formation). The well locations are shown in Fig. 1, with depth, total organic carbon (TOC), equivalent vitrinite reflectance, and mineralogy shown in Table 1.

3.1. Methane adsorption analysis

A high-pressure methane sorption apparatus was used to obtain storage capacity of powdered shale samples (at<60 mesh) which were initially dried at 105 °C. Methane adsorption measurements were then undertaken according to the step-by-step experimental prescriptions of Ji et al [37] as follows: (1) Each sample was then weighed and placed into cells at 0.1 °C and 0.1 psi accuracies. (2) An air tightness check of the adsorption setup was undertaken with helium gas at pressures up to 15 MPa, with pressure equilibration or tightness established if no pressure change is detected for 2 h at constant temperature. (3) Void volume within the sample cell is determined with helium. (4) Methane was introduced into the sample cell after evacuation of the adsorption apparatus. The molar volume was then obtained from measuring pressure before and after methane expansion into the sample cell. This was then used to obtain the amount of gas adsorbed at each pressure level. Isotherm measurement thus involved a repetition of these procedures until the highest pressure required for this study was achieved.

In this study, the Boyle's law gas adsorption isotherm measurement technique was used with the collected pressure points of each sample reaching 9 MPa (1300 psia), and the adsorption data obtained at 30 °C fitted with the Langmuir equation [38]. The model functions under the assumption that gas adsorption adheres to the monolayer adsorption theory with the ratio of the amount of adsorbed gas on the sorbent at a given pressure (P) to the Langmuir maximum adsorbed gas amount (Γ_{max}), is equivalent to the fractional surface covered [39]. Thus, the methane adsorption data obtained from the samples were fitted via [39]:

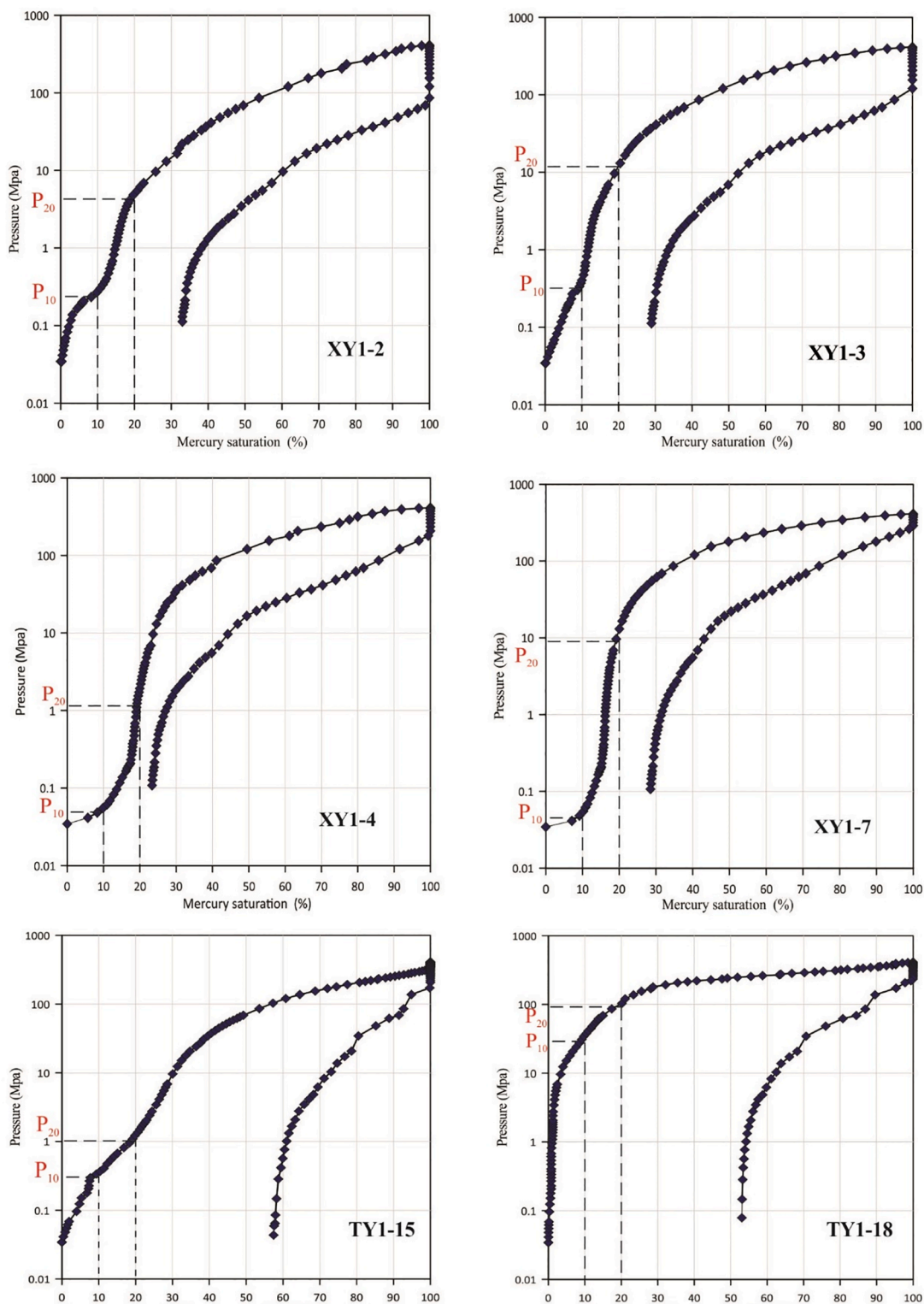$$\Gamma = \Gamma_{max}\frac{K \times P}{K \times P} \tag{1}$$

Table 4
Pore structure parameters along with measured and calculated pressure (P_{10}, $P_{10}CO_2$, P_{20}, $P_{20}CO_2$, and P_{50}) from MICP analysis.

Formation	Sample	Porosity (%)	Total pore volume (ml/g)	P_{10} (MPa)	P_{20} (MPa)	P_{50} (MPa)	D_{50} (nm)	P_{10} CO_2 (MPa)	P_{20} CO_2 (MPa)
Longmaxi	XY1-2	0.78	0.0046	0.297	5.306	84.185	14.51	0.0238	0.4245
	XY1-3	1.13	0.0066	0.471	10.593	145.184	8.41	0.0377	0.8474
	XY1-4	1.03	0.0061	0.061	2.166	152.322	8.02	0.0049	0.1733
	XY1-7	1.53	0.0090	0.0497	9.750	205.310	5.95	0.0040	0.7800
	TY1-15	5.13	0.0303	0.348	1.336	83.137	14.69	0.0278	0.1069
	TY1-18	2.62	0.0171	36.518	87.124	245.893	4.97	2.9214	6.9699
Niutitang	YK1-24	0.66	0.0039	0.13	0.619	38.577	31.66	0.0104	0.0495
	YK1-37	0.44	0.0026	0.061	0.089	1.533	796.66	0.0049	0.0071
	YK1-47	1.63	0.0096	0.076	0.183	72.11	16.94	0.0061	0.0146
	RY2-13	0.65	0.0044	0.0783	1.112	154.92	7.88	0.0063	0.0890
	RY1-6	0.62	0.0042	2.427	24.623	166.035	7.36	0.1942	1.9698
	RY1-8	0.6	0.0039	0.037	0.0671	127.194	9.60	0.0030	0.0054

Fig. 5. Capillary pressure curve from Longmaxi samples showing breakthrough pressure (P_{10}) and pressure at 20% saturation (P_{20}).

Where P is gas pressure (MPa), K is Langmuir constant (1/MPa) which is the Langmuir pressure constant (P_L, MPa) reciprocal and represents pressure at which gas storage capacity is equivalent to one-half of the maximum gas adsorption capacity. Eq. (1) was used with a least squares procedure to obtain the Langmuir parameters from the measured methane adsorption isotherm of each shale sample.

3.2. N_2 And CO_2 adsorption analyses

Low pressure CO_2 and N_2 adsorption of weighed powdered shale samples (180 – 250 μm particle size range) were respectively performed via the Quantachrome Autosorb-1 apparatus at the Beijing Center for Physical and Chemical Analysis, with experimental procedures prescribed by Sun et al [24]. This includes an initial degassing of crushed samples (40–80 mesh) at 110 °C under a 5-hour vacuum to remove
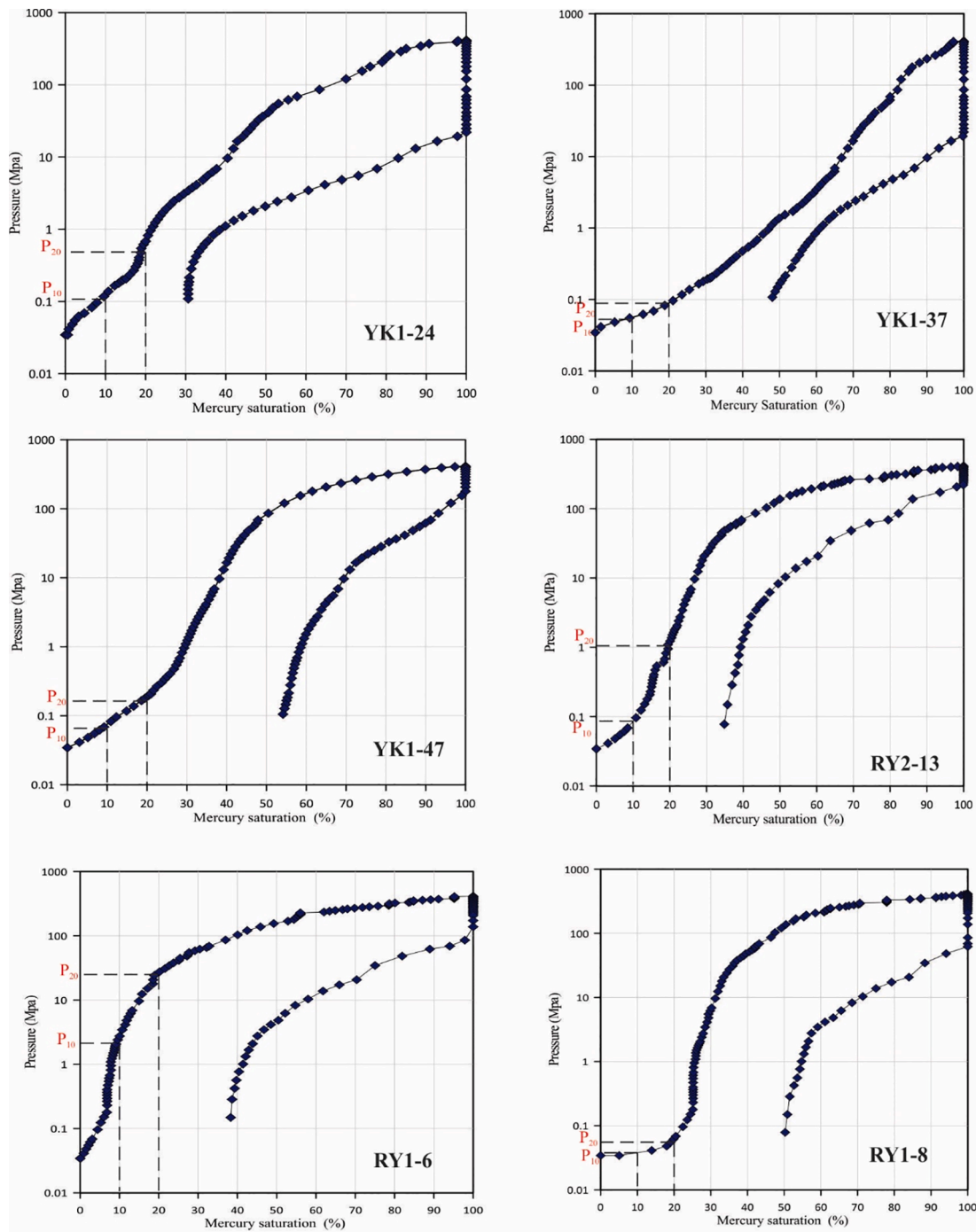
Fig. 6. Capillary pressure curve from Niutitang samples showing breakthrough pressure (P_{10}) and pressure at 20% saturation (P_{20}).

moisture, followed by measurement of nitrogen adsorption/desorption and carbon dioxide adsorption under relative pressures calibrated with the saturated vapor pressure of each gas. While nitrogen adsorption/ desorption isotherms were obtained at 77.3 K, carbon dioxide adsorption was undertaken at 0 °C with pressures up to 104.5 kPa.

Studies have argued that the preferred usage of CO_2 over N_2 for measuring the pore volume and pore size distribution of pores<2 nm is based on the gas having a higher accessibility for this pore size range compared to N_2 [40]. Thus, in this study, the density functional theory (DFT) was used to obtain micropore and mesopore volume from low pressure CO_2 and N_2 adsorption data. Nitrogen adsorption was also used to obtain the surface area via the Brunauer-Emmett-Teller (BET) model. The description of these models can be found in several literature [41-43].

3.3. Mercury capillary injection pressure (MICP)

MICP is based on the non-wetting mercury to imbibe the pore network bound to the sample boundaries [44]. Under an assumption of pores being cylindrically shaped, the pressure and pore throat diameter relationship is stated as [45]:

$$P = \frac{-2\sigma\cos\theta}{r} \qquad (2)$$

Where P represents the intrusive pressure; σ surface tension of mercury (0.48 N/m); θ mercury contact angle (130°); and r is the pore
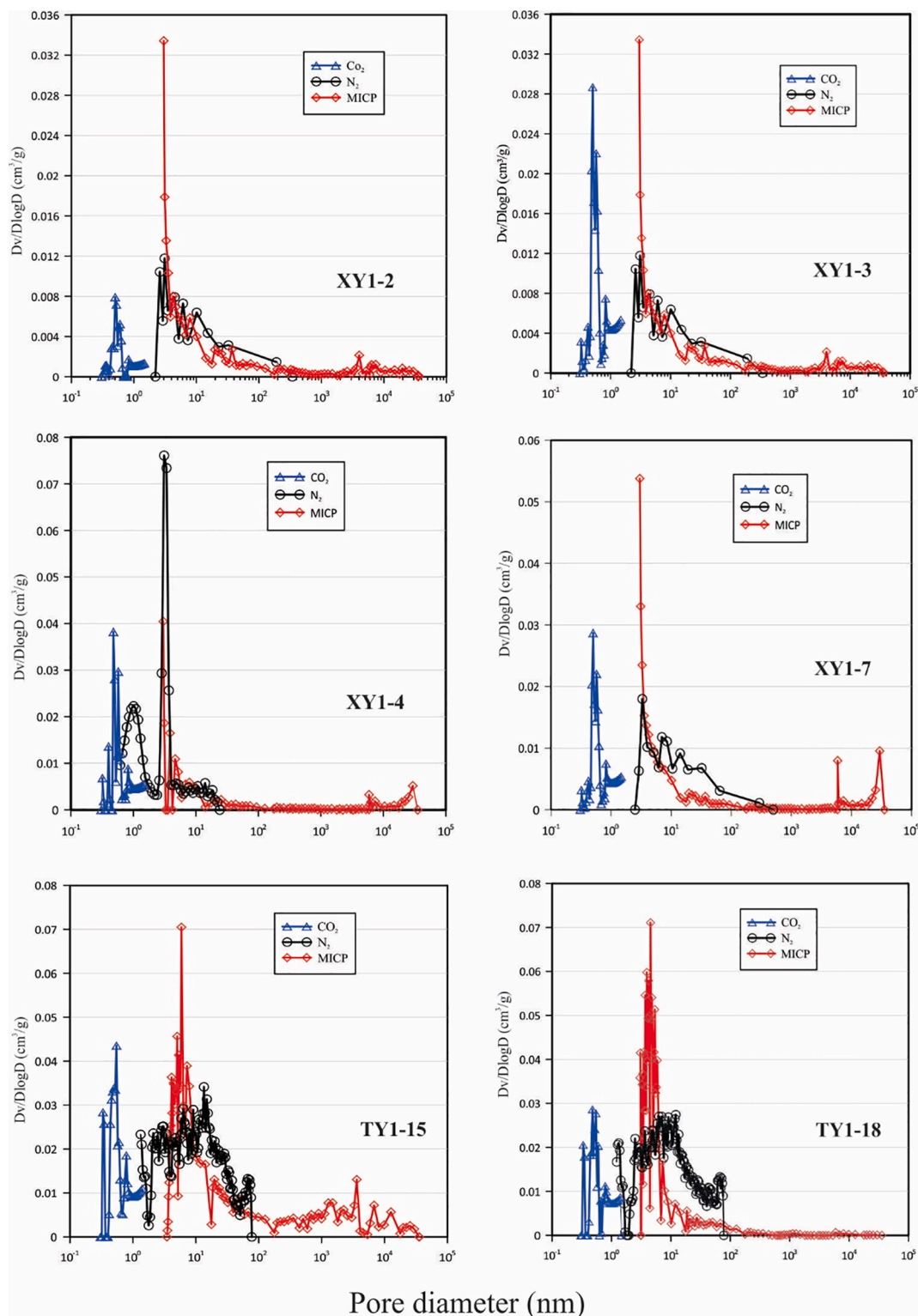
Fig. 7. Pore volume with pore size distributions obtained from MICP and low-pressure gas (CO_2 and N_2) sorption analysis of Longmaxi samples.

radius in nm.

Before MICP was conducted, the samples were cubically cut at 1 cm³ dimensions, polished on all surfaces before being oven dried at 60 °C for over 48 h, and cooled at room temperature within a desiccator. MICP analysis was then carried out via an intrusion porosimeter (Micromeritics Autopore IV 9520) with maximum pressure at 413 MPa (60,000 psia).

3.4. Multifractal analysis

Multifractal analysis considers the relationship between changes in the normalized probability distribution of a variable with a certain box size [46]. Thus, the box counting method which has been extensively used to evaluate the multifractal behaviour of low pressure CO_2 and N_2 adsorption data on shale samples [47,48], was used to evaluate our samples and the degree of heterogeneity in pore structure.
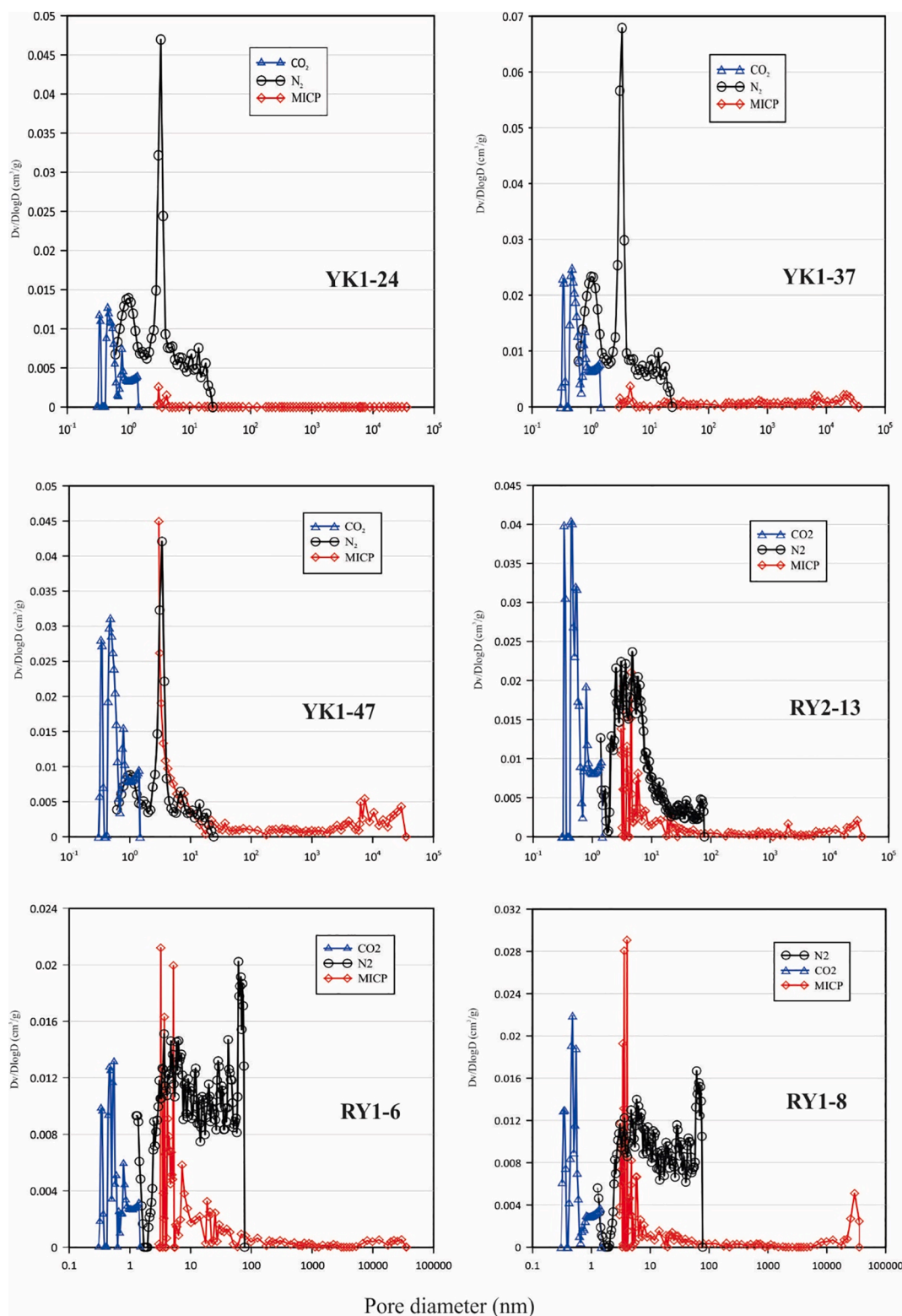
Fig. 8. Pore volume with pore size distributions obtained from MICP and low-pressure gas (CO_2 and N_2) sorption analysis of Niutitang samples.

This method is based on the variation of the number of different boxes (N_ε) of equal length, ε, required to cover the surface with ε^{-d_B}, where d_B is the measure to assess the fractal dimension [49]. In this study, N_ε represents the total number of boxes of length ε (taken as relative pressure P/P_0) required to cover the PSD curve, while the ith box probability mass function can be obtained via [47]:

$$p_i(\varepsilon) = N_i(\varepsilon)/N_T \tag{3}$$

where $N_i(\varepsilon)$ represents the ith box adsorbed nitrogen volume, and N_T the total adsorbed gas volume within the pores. Importantly, for each ε sized interval, $p_i(\varepsilon)$ can be defined with the following exponential form [47]:
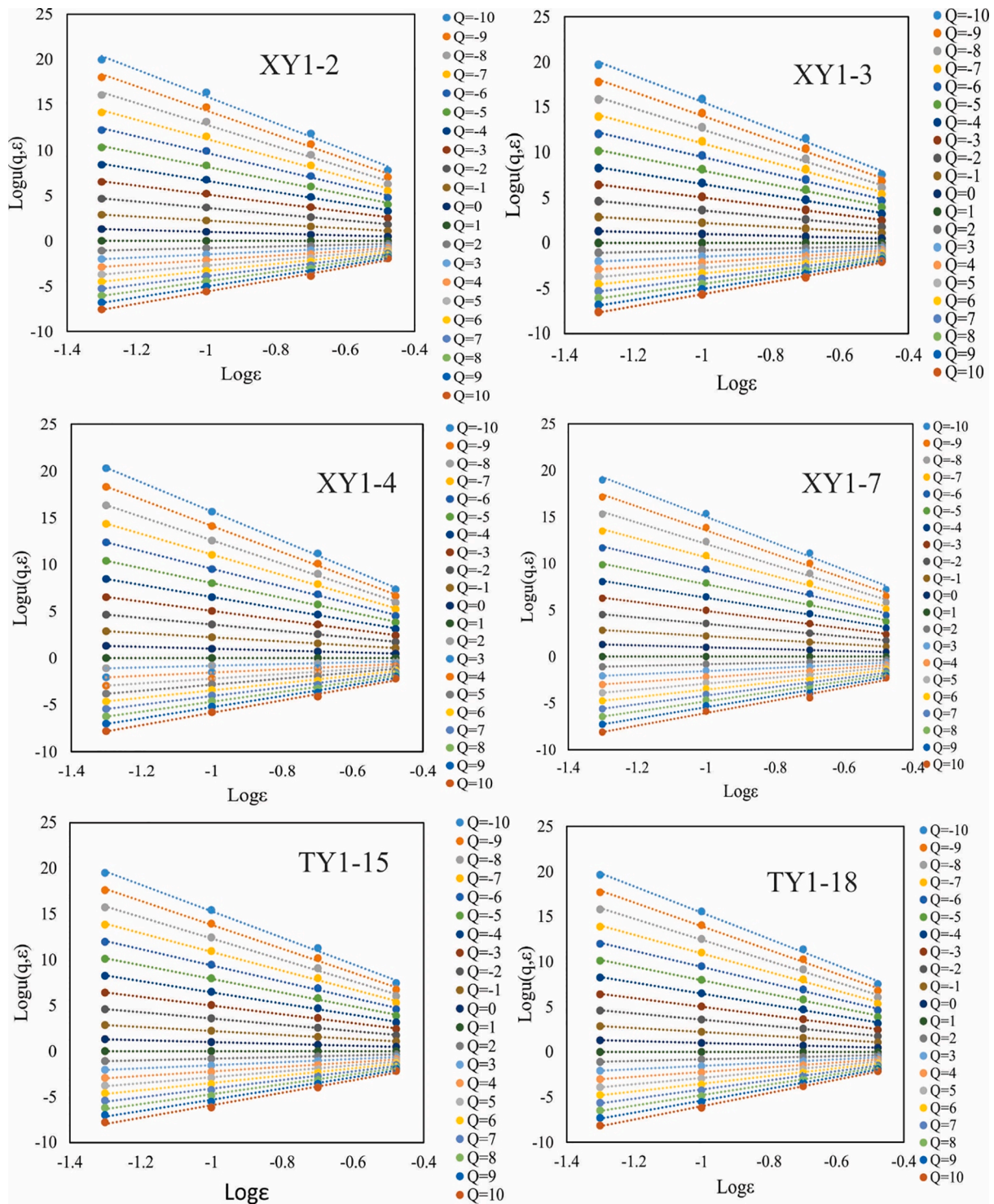
Fig 9. log–log plots of partition function against length for Longmaxi samples obtained from low pressure CO_2 adsorption isotherms.

$$p_i(\varepsilon) \ \varepsilon^{\alpha_i} \tag{4}$$

where α_i represents the singularity exponent which illuminates system singularities as they approach infinity with ε moves to 0 [50]. However, for intervals characterised by a multifractal property distribution, N_ε varies with ε according to a power law function which assumes the form [47]:

$$N_\alpha(\varepsilon) \ \varepsilon^{-f(\alpha)} \tag{5}$$

where $N_\alpha(\varepsilon)$ represents the number of boxes characterised by an ith

box probability mass function, $p_i(\varepsilon)$ having singularity strength within α and $\alpha + d\alpha$. Thus, $f(\alpha)$ can be used to represent the range of fractal dimensions linked to an abundance of the set with α singularity strength. This range, and $\alpha(q)$ can be calculated via [51]:

$$\alpha(q) \propto \frac{\left[\sum_{i=1}^{N(\varepsilon)} (u_i(q,\varepsilon) \times \ln p_i(\varepsilon))\right]}{\ln(\varepsilon)} \tag{6}$$
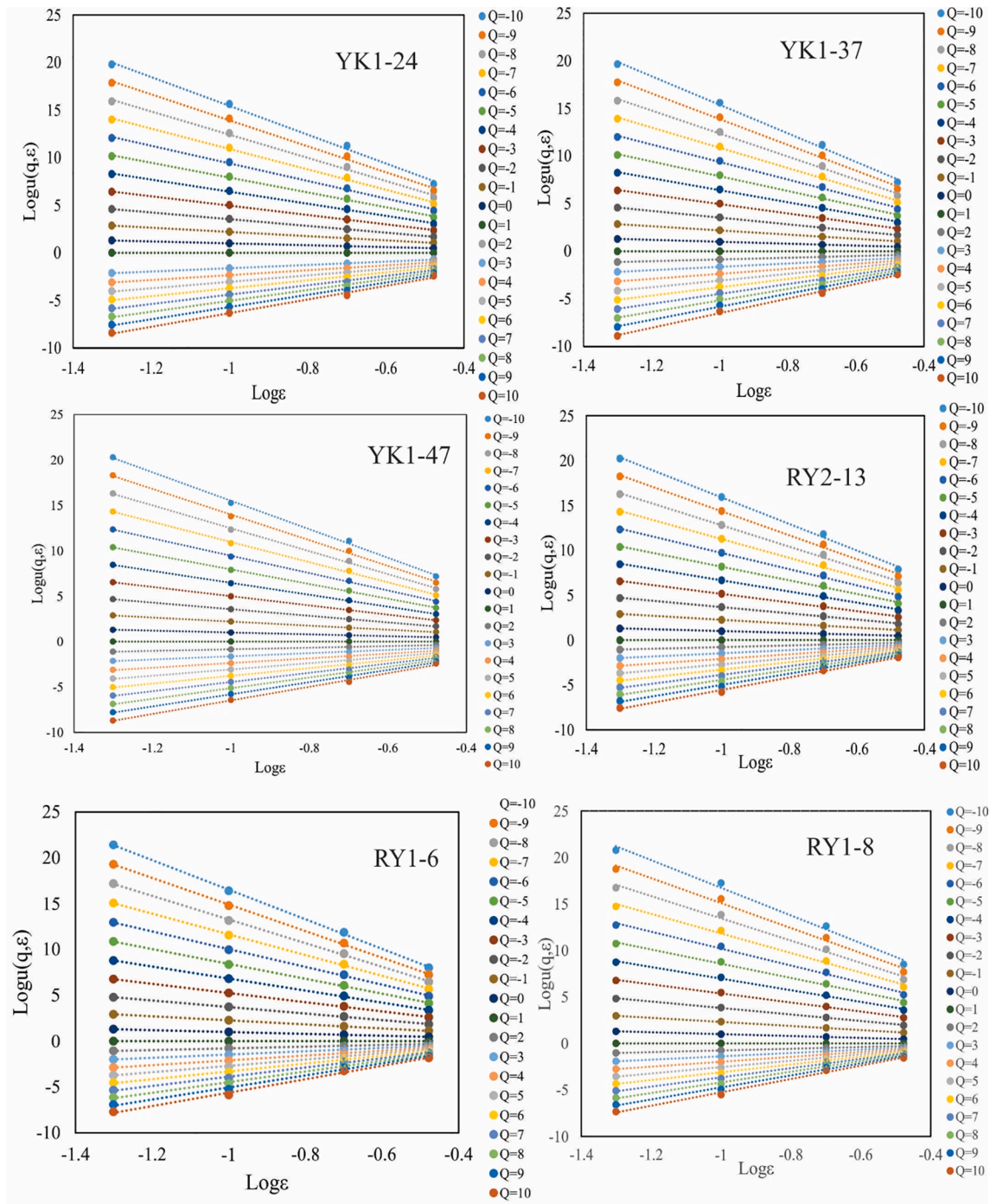
Fig 10. log–log plots of partition function against length for Niutitang samples obtained from low pressure CO_2 adsorption isotherms.

$$f(q) \propto \frac{\left[\sum_{i=1}^{N(\varepsilon)} \left(u_i(q,\varepsilon) \times \ln u_i(q,\varepsilon)\right)\right]}{\ln(\varepsilon)} \quad (7)$$

where:

$$u_i(q,\varepsilon) = \frac{P_i(\varepsilon)^q}{\sum_{i=1}^{N(\varepsilon)} P_i(\varepsilon)^q} \quad (8)$$

Here, q is an exponent used to express fractal properties in different scales. For every successive unit value of q from -10 to 10, the numerators in Eqs (6) and (7) are obtained with linear regression and are used to obtain $f(q)$ and $\alpha(q)$. It is important to note that a probability distribution function for multifractal applications is defined as [47]:

$$u_i(q,\varepsilon) = \sum_{i=1}^{N(\varepsilon)} P_i(\varepsilon)^q \ \varepsilon^{\tau(q)} \quad (9)$$

where τ_q represents the order q mass scaling function which is:

$$\tau(q) = \lim_{\varepsilon \to 0} \left[\ln \sum_i \frac{P_i(\varepsilon)^q}{\ln\left(\frac{1}{\varepsilon}\right)} \right] \quad (10)$$

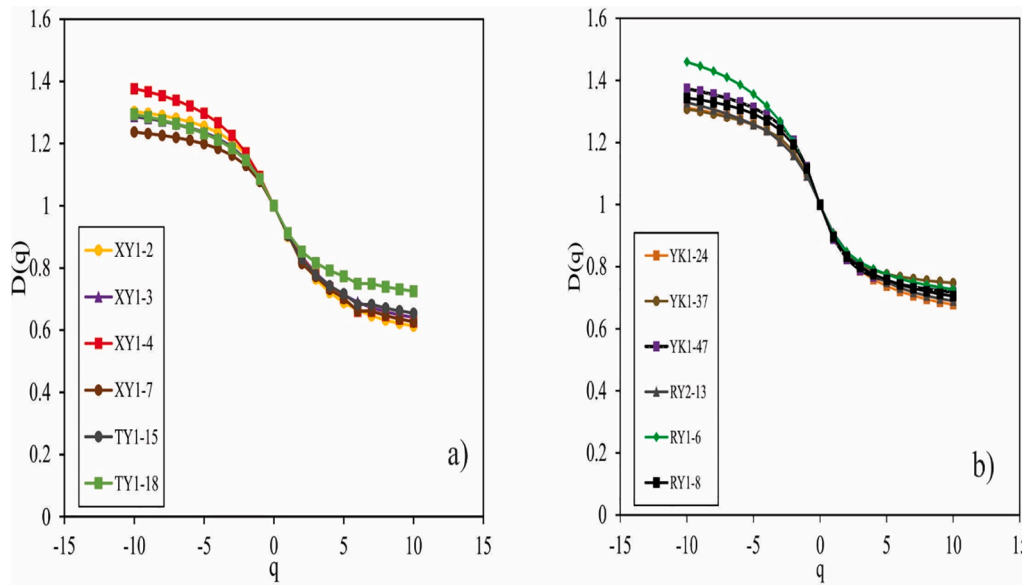Hence, D_q can be used to express a generalised dimension related to q via [47]:

Fig 11. Relationship between D_q and q from low pressure CO_2 adsorption isotherms for (a) Longmaxi and (b) Niutitang samples.

Table 5
Micropore generalized dimension characteristics obtained from low pressure CO_2 adsorption.

| Formation	Sample	D_{10+}	D_{10-}	D_0	D_1	D_2	D_0-D_1	H	$D_{10-}-D_{10+}$
Longmaxi	XY1-2	0.6134	1.3035	0.9997	0.9004	0.822	0.0993	0.911	0.6901
	XY1-3	0.6411	1.2869	0.9997	0.9083	0.8364	0.0914	0.9182	0.6458
	XY1-4	0.6269	1.3766	0.9997	0.908	0.8345	0.0917	0.91725	0.7497
	XY1-7	0.6264	1.2368	0.9997	0.9081	0.8141	0.0916	0.90705	0.6104
	TY1-15	0.6544	1.2907	0.9997	0.9039	0.8293	0.0958	0.91465	0.6363
	TY1-18	0.7251	1.294	0.9997	0.9126	0.8528	0.0871	0.9264	0.5689
Average		0.6479	1.2981	0.9997	0.9069	0.8315	0.0928	0.9158	0.6502
Niutitang	YK1-24	0.6777	1.3122	0.9997	0.8981	0.8294	0.1016	0.9147	0.6345
	YK1-37	0.7475	1.3073	0.9997	0.9024	0.8408	0.0973	0.9204	0.5598
	YK1-47	0.7178	1.3733	0.9997	0.8892	0.8235	0.1105	0.9118	0.6555
	RY2-13	0.6891	1.3292	0.9997	0.9091	0.8487	0.0906	0.9244	0.6401
	RY1-6	0.7267	1.4597	0.9997	0.9038	0.8475	0.0959	0.9238	0.733
	RY1-8	0.705	1.3432	0.9997	0.8952	0.8321	0.1045	0.9161	0.6382
Average		0.7106	1.3542	0.9997	0.8996	0.837	0.1001	0.9185	0.6435
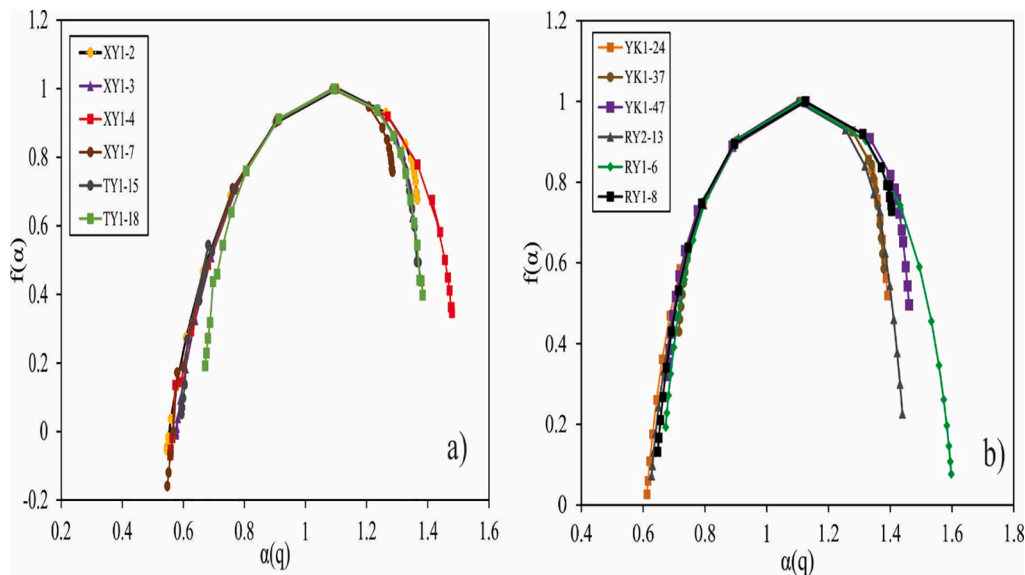
Fig 12. Multifractal singularity from low pressure CO_2 adsorption isotherms for (a) Longmaxi and (b) Niutitang samples.

Table 6
Micropore multifractal singularity characteristics obtained from low pressure CO_2 adsorption.

Formation	Sample	α_0	α_{10+}	α_{10-}	$\alpha_{10-} - \alpha_0$	$\alpha_{10-} - \alpha_{10+}$	R_d
Longmaxi	XY1-2	1.1035	0.5467	1.3661	0.2626	0.8194	0.2942
	XY1-3	1.0949	0.5762	1.355	0.2601	0.7788	0.2586
	XY1-4	1.0971	0.5573	1.4796	0.3825	0.9223	0.1573
	XY1-7	1.0891	0.5479	1.2847	0.1956	0.7368	0.3456
	TY1-15	1.0978	0.5941	1.3754	0.2776	0.7813	0.2261
	TY1-18	1.0936	0.6718	1.3836	0.29	0.7118	0.1318
Average		1.096	0.5823	1.3741	0.2781	0.7917	0.2356
Niutitang	YK1-24	1.1106	0.6126	1.3915	0.2809	0.7789	0.2171
	YK1-37	1.1082	0.7157	1.3795	0.2713	0.6638	0.1212
	YK1-47	1.1266	0.6781	1.461	0.3344	0.7829	0.1141
	RY2-13	1.0991	0.6275	1.4395	0.3404	0.812	0.1312
	RY1-6	1.1125	0.6733	1.598	0.4855	0.9247	−0.0463
	RY1-8	1.1246	0.6477	1.4032	0.2786	0.7555	0.1983
Average		1.1136	0.6592	1.4455	0.3319	0.7863	0.1226

$$D_q = \tau(q)/(q-1) \tag{11}$$

When q = 1, D_q will be defined as:

$$D_1 = \lim_{\varepsilon \to 0} \sum_{i=1}^{N(\varepsilon)} (P_i(\varepsilon) \ln P_i(\varepsilon))/\ln(\varepsilon) \tag{12}$$

4. Results

4.1. Organic geochemistry and mineralogy

Total organic carbon content and vitrinite reflectance (R_{oeq}) results obtained via procedures described in previous studies [24] are presented in Table 1 which reveals samples from both formations are characterized by TOC ranging from 1.02 wt% to 12.5 wt%, with the Longmaxi shale samples averaging lower at 3.33 wt% when compared to a 6.86 wt% TOC average for the Niutitang samples. Furthermore, Table 1 also explains that almost all samples have an R_{oeq} ranging from 1.95% to 3.89%. Alike the TOC results, the Longmaxi shales have a lower R_{oeq} with an average value of 2.42% compared to 3.26% from the Niutitang samples while both formations are in the gas generation window and overmature.

Table 1 infers that Longmaxi shale samples have a clay mineral content varying from 16 to 53 wt%, quartz from 20 wt% to 61 wt%, plagioclase from 3 wt% to 8 wt%, carbonate (calcite and dolomite) from 12 wt% to 50 wt%, along with traces of pyrite (from 1 wt% to 3 wt%) and K-feldspar. In comparison, the Niutitang shale samples had lower clay content, higher quartz, and a lack of K-feldspar. Furthermore, while both formations contain traces of pyrite, the Niutitang shale samples are attributed with lower carbonate mineral content and higher pyrite contents. These observed variations in mineralogical components between these two formations are similar to observations from previous comparative studies [25].

4.2. N₂ And CO₂ physisorption isotherms

N_2 adsorption and desorption isotherms (Fig. 2a, 2b) of the samples exhibits the existence of micropores and mesopores within the samples since the adsorption isotherms did not attain a full saturation with P/P_0 approaching 1.0. The morphology of the hysteresis loops obtained refers to the presence of ink-bottle and slit shaped pores based on recommendations by IUPAC [52]. The Niutitang shale samples are found more heterogenous in pore shape (having both ink-bottle and slit-shaped pore type hysteresis loops) (Fig. 2b), while Longmaxi shale samples are dominantly characterized by ink-bottle shaped pore (Fig. 2a). Furthermore, Table 2 explains that while mesopore volume and BET surface area of the Longmaxi shales respectively varies from 0.0073 ml/g to 0.031 ml/g and 12.55 m²/g to 39.20 m²/g, same parameters from the Niutitang shales vary from 0.016 ml/g to 0.028 ml/g, and 12.02 m²/g to

25.96 m²/g.

Low pressure CO_2 adsorption isotherms (Fig. 3a, 3b) obtained from the samples demonstrate type I characteristics according to the IUPAC classifications [52]. Furthermore, while micropore volume is observed to vary from 0.001 ml/g to 0.019 ml/g for the Longmaxi shales, it varies from 0.003 ml/g to 0.0086 ml/g for the Niutitang samples.

4.3. Methane sorption isotherms at 30 °C

Methane sorption isotherms were performed on shale samples at pressures up to approximately 9 MPa with temperature kept constant at 30 °C. While Langmuir fitting of experimentally measured methane sorption isotherms from both Longmaxi and Niutitang shale samples are shown in Fig. 4a and 4b, the Langmuir parameters that were found are summarized in Table 3.

This revealed a direct relationship between TOC and adsorbed methane volume for the sample from the formations, and also confirm that the amount of methane adsorbed per gram is generally larger for the Niutitang samples which are also characterized by a higher average (7.824 ml/g) of Langmuir maximum amount of adsorbed gas compared to 2.01 ml/g as the average value that is obtained from the Longmaxi samples. We infer a high maximum methane adsorption in both formations due to them being organic rich and clay poor (Table 3).

4.4. Pore structure and CO₂ breakthrough pressure from MICP

Pore structure parameters obtained from the samples via MICP are summarized in Table 4. Porosity for the Longmaxi samples is observed to vary from 0.78% to 5.13% and total pore volume from 0.0046 ml/g to 0.0303 ml/g. Breakthrough pressure (pressure at 10% mercury intrusion;[53]) (P_{10}) (Fig. 5, and Fig. 6) is also observed to vary from 0.0497 MPa to 36.518 MPa, median capillary pressure (P_{50}) from 83.137 MPa to 245.893 MPa, and median pore throat diameter (D_{50}) from 4.97 nm to 14.69 nm. In comparison, Niutitang shale samples are found to have lower porosity (0.60% to 1.63 %), total pore volume (0.0026 ml/g to 0.0096 ml/g), breakthrough pressure (P_{10}) (0.037 MPa to 2.427 MPa), and median capillary pressure (P_{50}) (1.533 MPa to 166.035 MPa). Moreover, samples from this formation are also observed on average to own a higher median pore diameter.

Pore size distribution plots (Fig. 7 and Fig. 8) obtained from the MICP and low-pressure gas sorption analysis of both formations reveal the presence of micropores and macropores, along with the abundance of peaks within the mesopore ranges.

Several studies have used CO_2 breakthrough pressure ascertained from MICP analysis to understand the interactions of CO_2 with shales, exclusively for the goal of CCS [54-56]. Thus, in order to evaluate the CO_2 sequestration suitability of the Longmaxi and Niutitang shale gas reservoirs, capillary pressure data obtained via MICP is converted to CO_2/brine data as follows [56]:
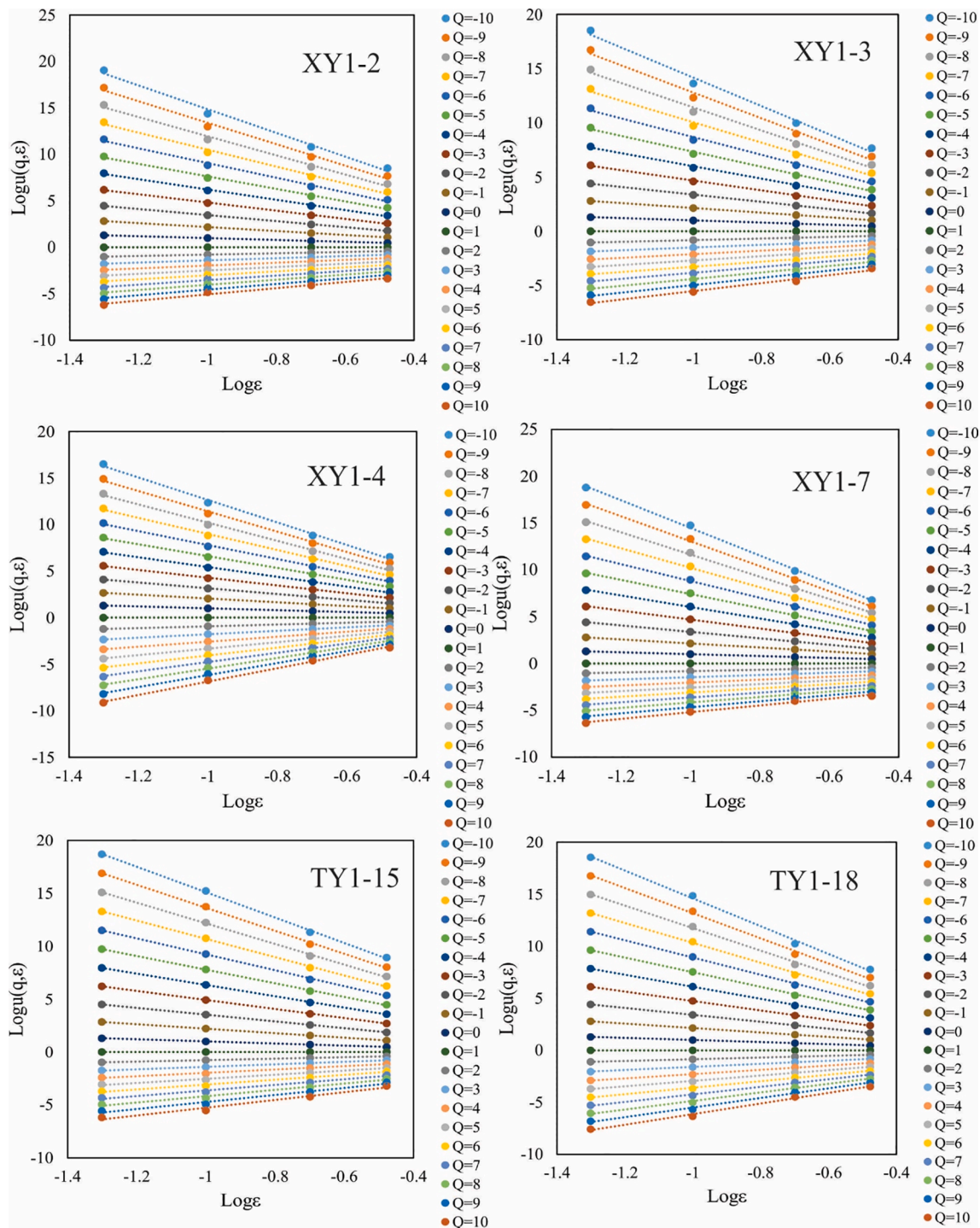
Fig 13. log–log plots of partition function against length for Longmaxi samples obtained from low pressure nitrogen adsorption isotherms.

$$P_{CO2-Brine} = 0.08 \times P_{C_{Hg-air}} \quad (13)$$

Where; $P_{CO2-Brine}$ represents CO_2 system capillary pressure, and $P_{C_{Hg-air}}$ the experimentally obtained capillary pressure. A comparison of calculated CO_2 breakthrough pressure for both formations (Table 4) show the Longmaxi samples having higher CO_2 breakthrough pressures on average.

4.5. Micropore (0.3 – 1.4 nm) multifractal features

Low pressure CO_2 adsorption isotherms obtained from the samples were used to derive log–log plots of the partition function $u(q,\varepsilon)$ vs. the length scale ε for q values ranging from −10 to 10 (at successive q = 1 intervals) (Fig. 9 and Fig. 10). The plots reveal the existence of a linear relationship between $\log u(q,\varepsilon)$ and $\log \varepsilon$ for all samples, thus exhibiting the multifractal behaviour of the micropore PSD curves. Furthermore, the linear trend lines are also observed to be respectively characterised by negative and positive slopes when q < 0 and q > 0.

The generalised dimensions D_q from low-pressure CO_2 adsorption data obtained from the samples were calculated from combining Eqs (11) and (12) is presented in Fig. 11a and Fig. 11b. The curves, along with the summarised data summarized in Table 5, all reveal a decrease in generalised dimension with increasing q which agrees with results
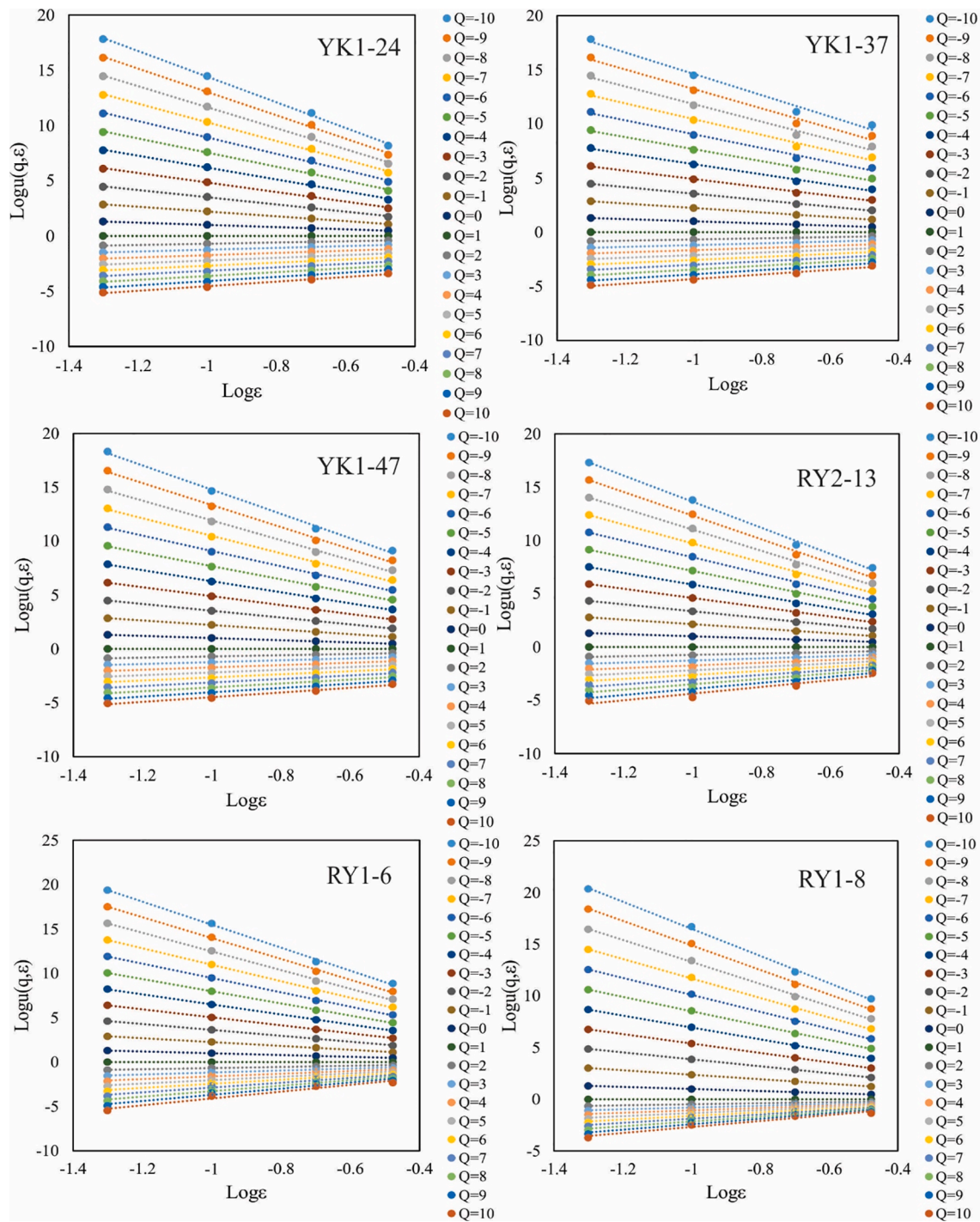
Fig 14. log–log plots of partition function against length for Niutitang samples obtained from low pressure nitrogen adsorption isotherms.

from Fig. 9 and Fig. 10. This further illuminates the multifractal behaviour of micropore PSD within the samples.

D_0 represents the fractal behavior of non-empty boxes characterised by a porosity under successive finer partitions that is not dependent on the probability of porosity within the box [47]. Table 5 reveals all samples as being characterised by the same D_0. Thus, since D_1 represents entropy information for PSD along pore size intervals, the degree of distribution uniformity for PSD across specific pore size ranges can be represented by the D_0-D_1 indicator [47,48]. Table 5 shows that the Niutitang samples are characterised by higher D_0-D_1 values (0.1001) on average compared to the Longmaxi samples (0.0928). This suggests that the micropore PSD style of the Niutitang formation is more clustered,

with PSD for the Longmaxi formation being more homogenous.

D_2 is known as the correlation dimension which factors the behaviour of the second sampling moments [47,48]. Furthermore, the Hurst exponent H which is defined by $(D_2 + 1)/2$, is an indication of the positive autocorrection intensity, and can be used to explain the pore connectivity across various pore size networks [47]. Table 5 reveals that the Longmaxi samples are averagely characterised by lower D_2 and H values than the Niutitang samples.

A subtraction of D_{10+} from D_{10-} can be used to examine the heterogeneity of microporosity distribution over the pore size range measured by low pressure CO_2 adsorption [47]. Table 5 reveals the level of heterogeneity in microporosity within the Longmaxi samples is higher than
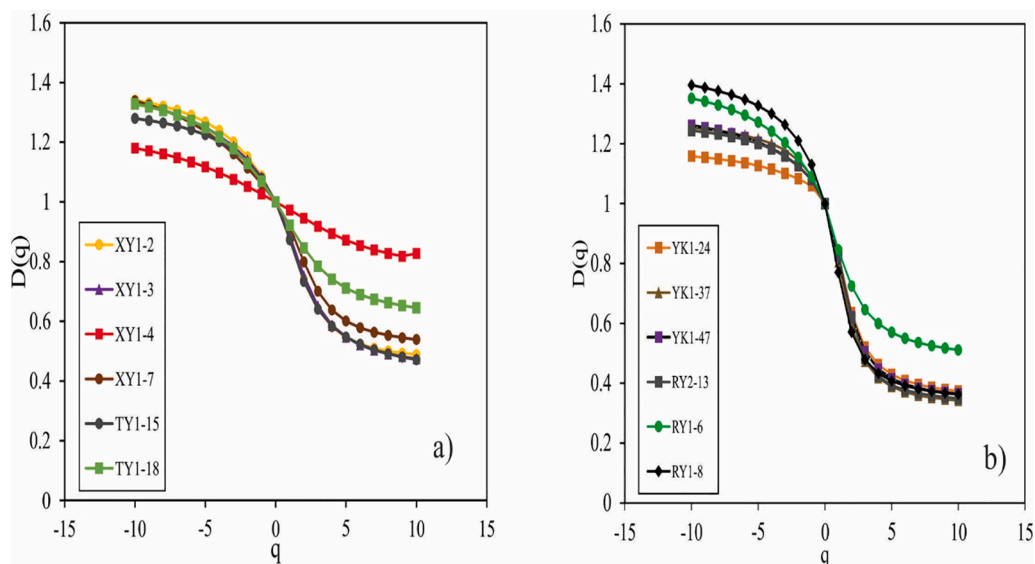
Fig 15. Relationship between D_q and q from low pressure nitrogen adsorption isotherms for (a) Longmaxi and (b) Niutitang samples.

Table 7
Mesopore-macropore generalized dimension characteristics obtained from low pressure nitrogen adsorption.

| Formation	Sample	D_{10+}	D_{10-}	D_0	D_1	D_2	D_0-D_1	H	D_{10-} -D_{10+}
Longmaxi	XY1-2	0.4887	1.341	0.9997	0.8772	0.7418	0.1225	0.8709	0.8523
	XY1-3	0.4748	1.3298	0.9997	0.8862	0.7525	0.1135	0.87625	0.8550
	XY1-4	0.8273	1.1797	0.9997	0.9728	0.9454	0.0269	0.9727	0.3524
	XY1-7	0.5388	1.3381	0.9997	0.9164	0.799	0.0833	0.8995	0.7993
	TY1-15	0.4719	1.2795	0.9997	0.8730	0.7338	0.1267	0.8669	0.8076
	TY1-18	0.6453	1.3280	0.9997	0.9219	0.8458	0.0778	0.9229	0.6827
Average		0.57447	1.29935	0.9997	0.90792	0.80305	0.09178	0.90152	0.72488
Niutitang	YK1-24	0.3739	1.1581	0.9997	0.8353	0.6359	0.1644	0.81795	0.7842
	YK1-37	0.3424	1.2534	0.9997	0.8050	0.589	0.1947	0.7945	0.9110
	YK1-47	0.3642	1.2611	0.9997	0.8252	0.6227	0.1745	0.81135	0.8969
	RY2-13	0.3490	1.2442	0.9997	0.8365	0.6173	0.1632	0.80865	0.8952
	RY1-6	0.5106	1.3517	0.9997	0.8455	0.7246	0.1542	0.8623	0.8411
	RY1-8	0.3629	1.3959	0.9997	0.7701	0.5703	0.2296	0.78515	1.0330
Average		0.38383	1.2774	0.9997	0.8196	0.62663	0.1801	0.81332	0.89357
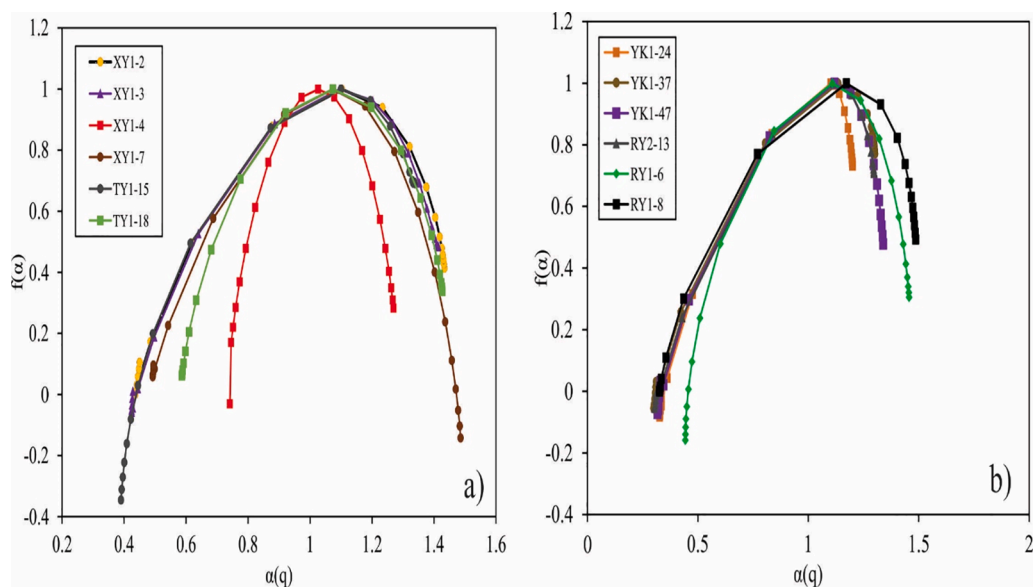
Fig 16. Multifractal singularity from low pressure nitrogen adsorption isotherms for (a) Longmaxi and (b) Niutitang samples.

Table 8
Mesopore-macropore multifractal singularity characteristics obtained from low pressure nitrogen adsorption.

Formation	Sample	α_0	α_{10+}	α_{10-}	α_{10-} -α_0	α_{10-} -α_{10+}	R_d
Longmaxi	XY1-2	1.1031	0.4504	1.4338	0.3307	0.9834	0.322
	XY1-3	1.0947	0.4284	1.4142	0.3195	0.9858	0.3468
	XY1-4	1.0264	0.7415	1.2694	0.2430	0.5279	0.0419
	XY1-7	1.0737	0.4946	1.4861	0.4124	0.9915	0.1667
	TY1-15	1.1002	0.3902	1.3384	0.2382	0.9482	0.4718
	TY1-18	1.0739	0.5869	1.4270	0.3531	0.8401	0.1339
Average		1.07867	0.51533	1.39482	0.31615	0.87948	0.24718
Niutitang	YK1-24	1.1020	0.3344	1.2007	0.0987	0.8663	0.6689
	YK1-37	1.1345	0.3113	1.3016	0.1671	0.9903	0.6561
	YK1-47	1.1188	0.331	1.3394	0.2206	1.0084	0.5672
	RY2-13	1.1116	0.3141	1.2977	0.1861	0.9836	0.6114
	RY1-6	1.1091	0.4437	1.4563	0.3472	1.0126	0.3182
	RY1-8	1.1724	0.3266	1.4862	0.3138	1.1596	0.5320
Average		1.12473	0.34352	1.34698	0.22225	1.00347	0.55897

Table 9
Partial least squares (PLS) parameters for Longmaxi samples.

Variable	Micropore index	Micropore Hurst exponent	Meso-macropore Index	Meso-macropore Hurst exponent
Intercept	0.7427303	0.9069510	1.2398563	0.8221223
TOC	−0.0010198	−0.0001833	−0.0117276	0.002584
Clay	−0.0000836	−0.0000150	0.0011537	−0.0002542
Carbonate	−0.0004856	−0.0000873	0.0020012	−0.0004409
Quartz	0.0004706	0.0000846	−0.0021161	0.0004662
Plagioclase	0.0070270	0.0012630	−0.0336555	0.0074155
Pyrite	0.0033641	0.0006046	−0.0573939	0.0126459

Table 10
Partial least squares (PLS) parameters for Niutitang samples.

Variable	Micropore index	Micropore Hurst exponent	Meso-macropore index	Meso-macropore Hurst exponent
Intercept	0.785236	0.9252754	0.6941024	0.8593773
TOC	−0.000007	0.0000443	0.0063120	−0.0009398
Clay	0.0000017	−0.0000105	−0.0001014	0.0000151
Carbonate	0.0000016	−0.0001007	−0.0062525	0.0009309
Quartz	−0.0000091	0.0000573	0.0012485	−0.0001859
Plagioclase	0.0000691	−0.0004381	0.0010267	−0.0001529
Pyrite	0.0001457	−0.0009229	0.0448645	−0.0066798

the Niutitang samples due to the former being characterised by higher D_{10-} - D_{10+} values on average. This also agrees with the previous observation of the Niutitang samples having a lower degree of PSD

heterogeneity.

Plots of $f(\alpha)$ vs. α for all samples (Fig. 12a and Fig. 12b) exhibit a strong asymmetric (as α approaches 1) convex parabolic shape, with all except the curve from sample RY1-6 having a positive slope section (left-hand side) that is wider than the negative slope section (right-hand side). While calculated fractal parameters from the plots reveal the Longmaxi samples are on average characterised by lower α_0, α_{10-}, α_{10+}, and α_{10-} -α_0 (Table 6). The Niutitang samples are also revealed to averagely possess lower α_{10-} -α_{10+}, and R_d (obtained from (α_0 -α_{10+}) − (α_{10-} -α_0)), with all except sample RY1-6 manifesting positive values of the latter. Furthermore, the observation of averagely higher α_0 in the Niutitang samples asserts using the Hurst exponent to suggest that compared to the Longmaxi samples, the concentration of PSD over a specific pore size range is of a higher level.

4.6. Mesopore-macropore (1.4 – 300 nm) multifractality

In order to evaluate the multifractal behavior of PSD in the mesopore-macropore range, isotherms from low pressure N_2 adsorption were used to obtain log–log plots of partition function $u(q,\varepsilon)$ vs. length scale ε from $q = -10$ to $q = 10$, at $q = 1$ successive intervals (Fig. 13 and Fig. 14). Following the plots from CO_2 adsorption (Fig. 9 and Fig. 10), the curves reveal a multifractal characteristic in the mesopore-macropore PSD. Other similarities include the proximity of regression lines, along with negative and positive slopes when $q > 0$ and $q < 0$.

The calculated generalised dimensions (Fig. 15a, Fig. 15b) decrease in D_q with increasing q. A comparison of generalised dimensions obtained from the samples (Table 7) reveal a similarity in D_0, along with averagely lower D_1, D_2, D_0-D_1, and H values in the Niutitang samples which are also characterised by larger D_{10-} -D_{10+} values on average.
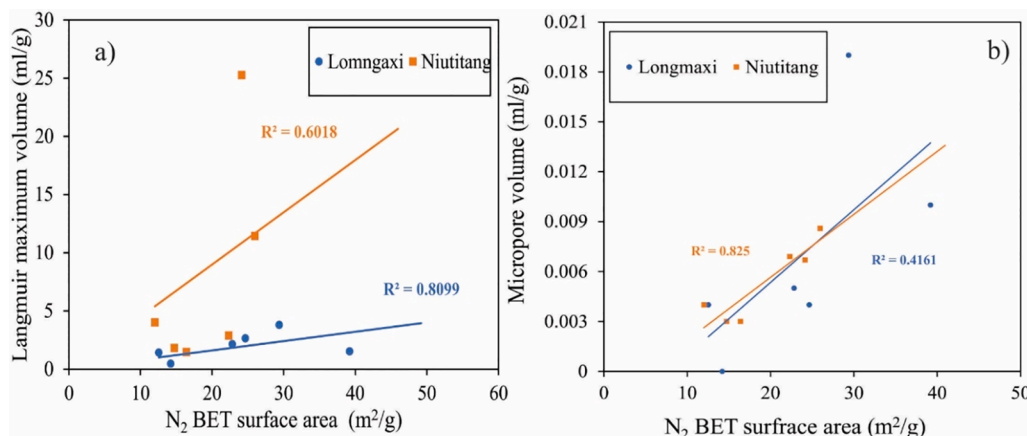
Fig. 17. Plots of (a) maximum adsorbed volume, and (b) CO_2 micropore volume against BET surface area.
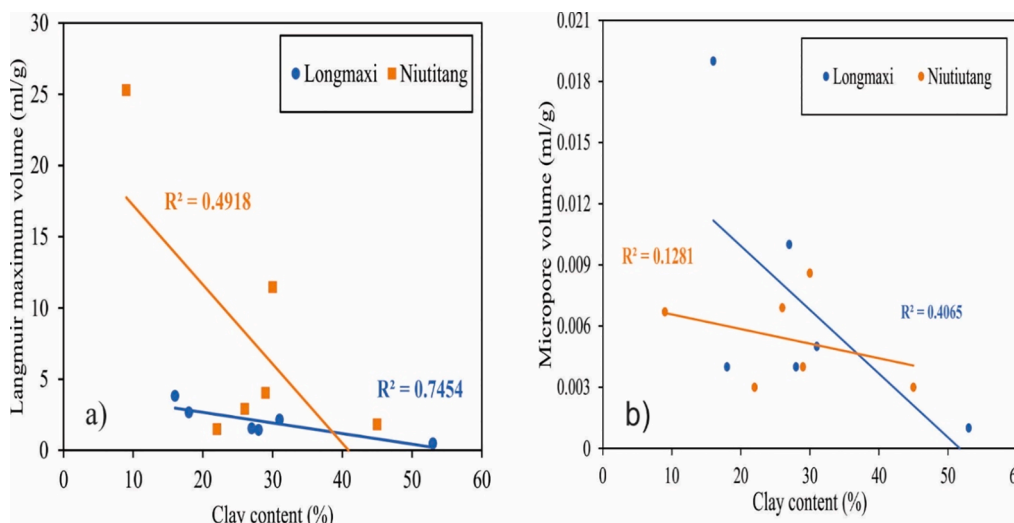
Fig. 18. Plot of (a) maximum adsorbed volume and (b) CO$_2$ micropore volume against clay content.
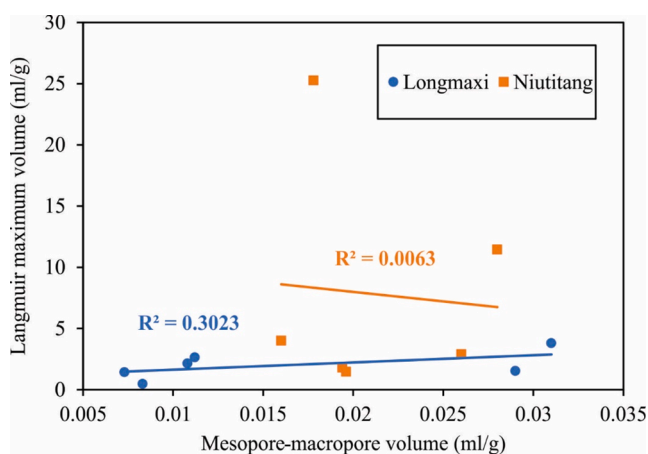

Fig. 19. Plot of maximum adsorbed volume against mesopore-macropore volume obtained from nitrogen adsorption.

While the D_0-D_1 and D_{10-} -D_{10+} observations respectively indicate the Niutitang samples are characterised by lower clustering of PSD and higher heterogeneous distribution of pores, the average variation of H values indicates that pore connectivity is better in the Longmaxi samples.

The multifractal behaviour of mesopore-macropore PSD is observed in the convex portion of the $f(\alpha)$ versus α plots for all samples (Fig. 16), with a comparison of the fractal parameters obtained (Table 8) revealing lower α_0, α_{10-} -α_{10+}, and R_d, values in the Longmaxi samples. These samples are also observed to own higher α_{10+}, α_{10-}, and α_{10-} -α_0 values. However, the average variation of α_0 means that our previous observation of the Longmaxi samples being characterised by a shorter range of PSD and more concentrated, the α_{10-} -α_{10+} average variation refers to a more homogenous nature. It is also important to note that positive R_d values obtained from all samples indicate a PSD mainly characterised by low probability areas.

5. Discussion

5.1. Pore heterogeneity controls and CO$_2$ storage implications

To understand how various parameters influence each other to control a particular phenomenon, partial least-squares regression (PLS)

have been used frequently to ascertain the dependency of shale pore heterogeneity on inorganic and organic constituent components [47]. In this study, in order to evaluate how mineralogical and organic matter content controls pore heterogeneity in both formations, PLS was applied to the data from both formations with rock compositions (K-feldspar excluded since samples are deficient) set as independent variables, and Hurst exponent set as a dependent component. Table 9 reveals that while the connectivity of micropores and mesopore-macropores in the Longmaxi samples slightly increases with organic carbon content, quartz, plagioclase, and pyrite, clays and carbonate are observed to have a negative impact. Furthermore, apart from organic matter content which slightly reduces the heterogeneity of both micropores and mesopore-macropores, minerals have an opposite effect on micropore and mesopore-macropore degree of heterogeneity. For instance, minerals which slightly increase micropore heterogeneity (that is, quartz, plagioclase, and pyrite), slightly reduce mesopore-macropore heterogeneity. Furthermore, carbonate slightly is found to reduce micropore heterogeneity while having an opposite influence on mesopore-macropore heterogeneity.

In comparison to the Longmaxi samples, PLS results from the Niutitang samples summarised in Table 10 demonstrate that plagioclase and pyrite respectively slightly increase and reduce the heterogeneity and connectivity of both micropore and mesopore-macropores. Micropore heterogeneity and mesopore-macropore connectivity slightly increases with clay and carbonate, which both slightly reduce micropore connectivity. Furthermore, TOC and quartz are both observed to slightly reduce micropore heterogeneity and mesopore-macropore connectivity. Both components are also slightly increase micropore connectivity.

Other studies have used electron microscopy to reveal that compared to the Niutitang shale, Longmaxi shales have a better pore connectivity via the porosity within clay minerals which connects surrounding organic matter pores [19]. Our findings also support a link between clay and organic microporosity for only the Longmaxi formation, which compared to the Niutitang formation is characterised by slight reductions in micropore heterogeneity and connectivity due to clay and organic matter. This is because, the Niutitang formation is attributed by a slight reduction and increase in micropore heterogeneity and connectivity due to the presence of organic micropores alike the Bakken formation [47]. The difference between inorganic and organic microporosity in both formations can be referred to a variation in diagenetic evolution [25], which studies have linked to a variation in the restriction of marine deposition for both formations [34].

CO$_2$ injection in shale reservoirs starts from hydraulic fractures to microcracks and macropores, before migrating to the mesopores and
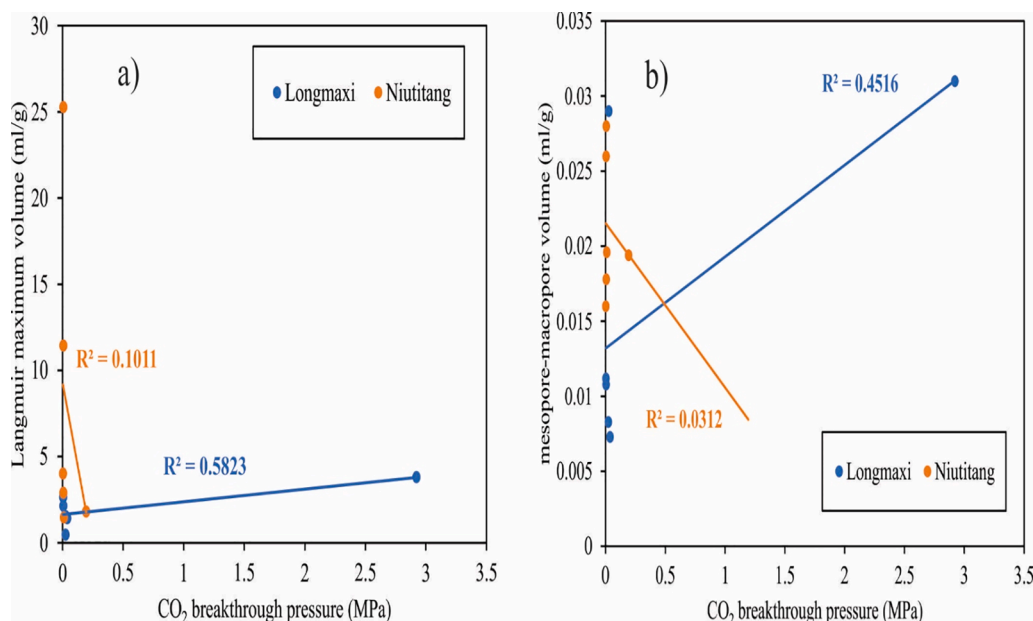
Fig. 20. Plot of (a) maximum adsorbed volume and (b) mesopore-macropore volume (N_2 adsorption) against CO_2 breakthrough pressure (P_{10} CO_2) calculated from MICP.
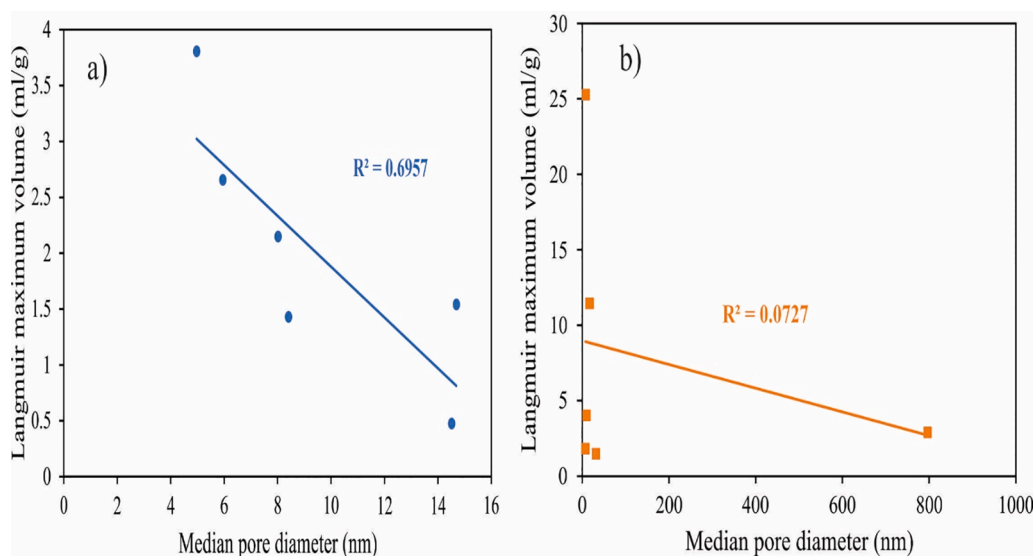

Fig. 21. Plot of maximum adsorbed volume against median pore diameter (D_{50}) obtained from MICP for (a) Longmaxi and (b) Niutitang samples.

micropores where the gas is stored in free state in the pore space and adsorbed on the surface of the pores [57]. Thus, the higher connectivity and PSD homogeneity observed in mesopore-macropores of the Long-maxi samples analysed in this study indicates a less complicated CO_2 migration process for the formation compared to the Niutitang formation. This, along with carbonate rich shales being prone to meso and micro porosity changes from CO_2 and water interactions which is found to increase available pore space for CO_2 storage [58,59], suggests a superior suitability of the carbonate rich Longmaxi samples over the Niutitang samples for CO_2 storage. We should emphasize that caprock integrity and the capability of the layers above the formation to contain stored CO_2, is a different story that needs a separate study based on the column of CO_2 in the above caprock layers.

5.2. Methane adsorption controls and CO_2 EGR implications

In shale gas reservoirs, gas stored in the adsorbed phase comprises 20–80% of total gas in place [60], hence the usage of CO_2 for EGR is based on the displacement of adsorbed methane within the pores. This displacement is controlled by the higher affinity of shales to CO_2 compared to methane, with several studies noting the dominant influence of clay minerals and organic matter on methane and CO_2 adsorption mechanisms and quantities [10,11].

In this study, although a direct relationship between TOC and gas adsorption was recognized which agrees with previous investigations of both formations [25], plots of nitrogen BET surface area vs. maximum adsorbed gas volume (Fig. 17a), and micropore volume (Fig. 17b), along with a plot of maximum adsorbed gas volume vs. clay content (Fig. 18a) all point to the fact that adsorption within the Niutitang formation is less influenced by the clay content. This observation is also supported by the

positive relationship between clay content and micropore volume only observed for the Longmaxi samples (Fig. 18b). Similarly slight reduction in micropore heterogeneity and connectivity due to clay content means that gas adsorption in the Longmaxi Formation can be impacted by the microporosity between clay platelet surfaces.

However, studies have also observed that gas storage within shale reservoirs that are not highly organic rich is less controlled by adsorption in the micropores and more by the bulk and adsorbed gas in the mesopore-macropore [61]. In this study, a plot of adsorbed volume vs. mesopore-macropore volume obtained from nitrogen adsorption (Fig. 19) shows a positive relationship only for samples from the Longmaxi formation which indicates a higher gas storage capacity compared to the Niutitang shale.

CO_2 EGR is done to increase gas production by displacing adsorbed gas through CO_2 injection into the formation [62]. In this study, our experimental observations of a positive relationship between adsorbed methane volume with CO_2 breakthrough pressure and median pore diameter (D_{50}) (Fig. 20a and Fig. 21a) for the Longmaxi shale samples verifies that migration of CO_2 into the reservoir pore space will be inhibited by methane adsorbed within the mesopore-macropores. This observation which is also supported by a positive relationship between mesopore-macropore volume and CO_2 breakthrough pressure for the Longmaxi samples (Fig. 20b), denotes that when CO_2 EGR is undertaken within the Longmaxi formation, a displacement of this adsorbed methane by the injected CO_2 will result in methane recovery and an availability of pore space for CO_2 storage. Collectively, suitability of Longmaxi compared to the Niutitang shale for CO_2 EGR is found from this study while further and larger scale analysis is necessary to make robust conclusions.

6. Conclusion

A comparative analysis of pore structure and composition for the final goal of influencing CO_2 storage within the Longmaxi and Niutitang shale gas reservoirs is carried out via adsorption experiments and MICP with the following conclusions and recommendations:

1. Clay and TOC controls on micropore heterogeneity and connectivity are only observed in the Longmaxi Formation. Thus, while organic carbon content plays a role on gas adsorption in both formations, clay content controls are also observed for the Longmaxi formation.
2. Higher gas storage capacity in the Longmaxi formation is attributed to gas stored in mesopore-macropores, confirmed by positive relationship between adsorbed volume with mesopore-macropore volume.
3. Increased migration of CO_2 into the Longmaxi Formation pore network is expected due to higher connectivity and higher degree of PSD homogeneity of mesopore-macropores in the formation.
4. Positive relationships are obtained from adsorbed gas volume with CO_2 breakthrough pressure and median pore diameter plots. This, along with a positive relationship between mesopore-macropore volume and CO_2 breakthrough pressure, suggests that CO_2 migration into reservoir pore space of the Longmaxi Formation will be inhibited by a displacement of methane adsorbed in mesopore-macropores.
5. Collectively we recommend the Longmaxi Formation over the Niutitang for CO_2 storage and EGR considering the results from the detailed studies on the pore structure of these two major shale gas plays in China.

Declaration of Competing Interest

The authors declare that they have no known competing financial interests or personal relationships that could have appeared to influence the work reported in this paper.

References

[1] Li Q, Chen ZA, Zhang J-T, Liu L-C, Li XC, Jia L. Positioning and revision of CCUS technology development in China. Int J Greenh Gas Control 2016;46:282–93.
[2] World Meteorological Organization. The State of Greenhouse Gases in the Atmosphere Based on Global Observations through 2019. WMO Greenhouse Gas Bulletin 2020:16. https://library.wmo.int/doc_num.php?explnum_id=10437; 2020.
[3] Wu H, Zheng L-X. Empirical Study on China's Energy Development under the Target of Carbon Emissions. IOP Conf Ser: Earth Environ Sci 2020;446(2):022045.
[4] Zong J, Sun L, Bao W. Research of present status and development suggestions regarding the carbon capture, utilization and storage. IOP Conf Ser: Earth Environ Sci 2020;510(4):042001.
[5] Xu T, Tian H, Zhu H, Cai J. Advances in China actively promotes CO_2 capture, utilization and storage research to achieve carbon peak and carbon neutrality. Adv Geo-Energy Res 2022;6:1–3.
[6] Malischek R, McCulloch S. The world has vast capacity to store CO_2: Net zero means we'll need it. Int Energy Agency Comment 2021.
[7] Raza A, Gholami R, Rezaee R, Rasouli V, Rabiei M. Significant aspects of carbon capture and storage – A review. Petroleum 2019;5:335–40. https://doi.org/10.1016/j.petlm.2018.12.007.
[8] Hong L, Jain J, Romanov V, Lopano C, Disenhof C, Goodman A, et al. An investigation of factors affecting the interaction of CO_2 and CH_4 on shale in Appalachian Basin. J Unconv Oil Gas Resour 2016;14:99–112. https://doi.org/10.1016/j.juogr.2016.02.003.
[9] Godec M, Koperna G, Petrusak R, Oudinot A. Assessment of factors influencing CO_2 storage capacity and injectivity in Eastern U.S. gas shales. Energy Procedia, vol. 37, Elsevier Ltd; 2013, p. 6644–55. https://doi.org/10.1016/j.egypro.2013.06.597.
[10] Schepers KC, Nuttall B, Oudinot AY, Gonzalez R. Reservoir modeling and simulation of the devonian gas shale of eastern Kentucky for enhanced gas recovery and CO_2 storage. SPE Int. Conf. CO_2 Capture, Storage, Util. 2009, Society of Petroleum Engineers; 2009, p. 154–73. https://doi.org/10.2118/126620-ms.
[11] Kang SM, Fathi E, Ambrose RJ, Akkutlu IY, Sigal RF. Carbon dioxide storage capacity of organic-rich shales. Proc. - SPE Annu. Tech. Conf. Exhib., vol. 4, 2010, p. 3000–16. https://doi.org/10.2118/134583-ms.
[12] Zhou J, Hu N, Xian X, Zhou L, Tang J, Kang Y, et al. Supercritical CO_2 fracking for enhanced shale gas recovery and CO_2 sequestration: Results, status and future challenges. Adv Geo-Energy Res 2019;3:207–24. https://doi.org/10.26804/AGER.2019.02.10.
[13] Jia B, Tsau JS, Barati R. A review of the current progress of CO_2 injection EOR and carbon storage in shale oil reservoirs. Fuel 2019;236:404–27. https://doi.org/10.1016/j.fuel.2018.08.103.
[14] Zhou J, Xie S, Jiang Y, Xian X, Liu Q, Lu Z, et al. Influence of supercritical CO_2 exposure on CH_4 and CO_2 adsorption behaviors of shale: implications for CO_2 sequestration. Energy Fuels 2018;32:6073–89. https://doi.org/10.1021/acs.energyfuels.8b00551.
[15] Cheng Y, Zeng M, Lu Z, Du X, Yin H, Yang L. Effects of supercritical CO_2 treatment temperatures on mineral composition, pore structure and functional groups of shale: Implications for CO_2 sequestration. Sustain 2020;12. https://doi.org/10.3390/su12093927.
[16] Huang X, Zhao YP, Wang X, Pan L. Adsorption-induced pore blocking and its mechanisms in nanoporous shale due to interactions with supercritical CO_2. J Pet Sci Eng 2019;178:74–81. https://doi.org/10.1016/j.petrol.2019.03.018.
[17] Rezaee R, Saeedi A, Iglauer S, Evans B. Shale alteration after exposure to supercritical CO_2. Int J Greenh Gas Control 2017;62:91–9. https://doi.org/10.1016/j.ijggc.2017.04.004.
[18] Gasparik M, Bertier P, Gensterblum Y, Ghanizadeh A, Krooss BM, Littke R. Geological controls on the methane storage capacity in organic-rich shales. Int J Coal Geol 2014;123:34–51. https://doi.org/10.1016/j.coal.2013.06.010.
[19] Sun M, Yu B, Hu Q, Yang R, Zhang Y, Li B. Pore connectivity and tracer migration of typical shales in south China. Fuel 2017;203:32–46. https://doi.org/10.1016/j.fuel.2017.04.086.
[20] Gao Z, Fan Y, Hu Q, Jiang Z, Cheng Y. The effects of pore structure on wettability and methane adsorption capability of longmaxi formation shale from the southern Sichuan Basin in China. Am Assoc Pet Geol Bull 2020;104:1375–99. https://doi.org/10.1306/01222019079.
[21] Wang Y, Liu L, Sheng Y, Wang X, Zheng S, Luo Z. Investigation of Supercritical Methane Adsorption of Overmature Shale in Wufeng-Longmaxi Formation, Southern Sichuan Basin. China Energy and Fuels 2019;33:2078–89. https://doi.org/10.1021/acs.energyfuels.8b04344.
[22] Lin T, Bao S, Zhang J, Zhou Z, Yuan K, Li Bo, et al. Shale gas accumulation conditions and gas-bearing characteristics of the Lower Cambrian Niutitang Formation in Well Changye-1 in northwestern Hunan Province. Pet Res 2016;1(2): 205–12.
[23] Xi Z, Tang S, Wang J, Yi J, Guo Y, Wang K. Pore structure and fractal characteristics of niutitang shale from China. Minerals 2018;8(4):163.

[24] Sun M, Yu B, Hu Q, Chen S, Xia W, Ye R. Nanoscale pore characteristics of the Lower Cambrian Niutitang Formation Shale: A case study from Well Yuke #1 in the Southeast of Chongqing. China Int J Coal Geol 2016;154–155:16–29. https://doi.org/10.1016/j.coal.2015.11.015.

[25] Wang R, Hu Z, Sun C, Liu Z, Zhang C, Gao B, et al. Comparative analysis of shale reservoir characteristics in the Wufeng-Longmaxi (O_3w-S_1l) and Niutitang (ϵ_1n) Formations: A case study of wells JY1 and TX1 in the southeastern Sichuan Basin and its neighboring areas, southwestern China. Interpretation 2018;6:SN31–45.. https://doi.org/10.1190/int-2018-0024.1.

[26] Tan J, Horsfield B, Mahlstedt N, Zhang J, di Primio R, Vu TAT, et al. Physical properties of petroleum formed during maturation of Lower Cambrian shale in the upper Yangtze Platform, South China, as inferred from PhaseKinetics modelling. Mar Pet Geol 2013;48:47–56.

[27] Li A, Ding W, Jiu K, Wang Z, Wang R, He J. Investigation of the pore structures and fractal characteristics of marine shale reservoirs using NMR experiments and image analyses: A case study of the Lower Cambrian Niutitang Formation in northern Guizhou Province. South China Mar Pet Geol 2018;89:530–40. https://doi.org/10.1016/j.marpetgeo.2017.10.019.

[28] Chen S, Zhu Y, Wang H, Liu H, Wei W, Fang J. Shale gas reservoir characterisation: A typical case in the southern Sichuan Basin of China. Energy 2011;36:6609–16. https://doi.org/10.1016/j.energy.2011.09.001.

[29] Zou CN, Dong DZ, Yang H, Wang YM, Huang JL, Wang SF, et al. Conditions of shale gas accumulation and exploration practices in China (in Chinese with English abstract). Nat Gas Ind 2011;31:26–39.

[30] Dong D, Shi Z, Guan Q, Jiang S, Zhang M, Zhang C, et al. Progress, challenges and prospects of shale gas exploration in the Wufeng-Longmaxi reservoirs in the Sichuan Basin. Nat Gas Ind B 2018;5(5):415–24.

[31] Jiang S, Zhang J, Jiang Z, Xu Z, Cai D, Chen L, et al. Geology, resource potentials, and properties of emerging and potential China shale gas and shale oil plays. Interpretation 2015;3(2):SJ1–13.

[32] Zeng W, Zhang J, Ding W, Zhao S, Zhang Y, Liu Z, et al. Fracture development in Paleozoic shale of Chongqing area (South China). Part one: Fracture characteristics and comparative analysis of main controlling factors. J Asian Earth Sci 2013;75:251–66.

[33] Hao F, Zou H, Lu Y. Mechanisms of shale gas storage: Implications for shale gas exploration in China. Am Assoc Pet Geol Bull 2013;97:1325–46. https://doi.org/10.1306/02141312091.

[34] Tan J, Horsfield B, Fink R, Krooss B, Schulz H-M, Rybacki E, et al. Shale gas potential of the major marine shale formations in the upper yangtze platform, South China, Part III: Mineralogical, lithofacial, petrophysical, and rock mechanical properties. Energy Fuels 2014;28(4):2322–42.

[35] Yang C, Zhang J, Tang X, Ding J, Zhao Q, Dang W, et al. Comparative study on micro-pore structure of marine, terrestrial, and transitional shales in key areas. China Int J Coal Geol 2017;171:76–92.

[36] Li X, Zhang J, Wang Y, Guo M, Wang Z, Wang F. Accumulation condition and favorable area evaluation of shale gas from the Niutitang Formation in northern Guizhou. South China J Nat Gas Geosci 2018;3:1–10. https://doi.org/10.1016/j.jnggs.2018.03.001.

[37] Ji W, Song Y, Jiang Z, Wang X, Bai Y, Xing J. Geological controls and estimation algorithms of lacustrine shale gas adsorption capacity: A case study of the Triassic strata in the southeastern Ordos Basin. China Int J Coal Geol 2014;134–135:61–73. https://doi.org/10.1016/j.coal.2014.09.005.

[38] Langmuir I. The adsorption of gases on plane surfaces of glass, mica and platinum. J Am Chem Soc 1918;40:1361–403. https://doi.org/10.1021/ja02242a004.

[39] Ji L, Zhang T, Milliken KL, Qu J, Zhang X. Experimental investigation of main controls to methane adsorption in clay-rich rocks. Appl Geochemistry 2012;27:2533–45. https://doi.org/10.1016/j.apgeochem.2012.08.027.

[40] Sun M, Yu B, Hu Q, Zhang Y, Li Bo, Yang R, et al. Pore characteristics of Longmaxi shale gas reservoir in the Northwest of Guizhou, China: Investigations using small-angle neutron scattering (SANS), helium pycnometry, and gas sorption isotherm. Int J Coal Geol 2017;171:61–8.

[41] Gregg SJ, Sing KSW. Adsorption. Surface Area and Porosity. Second Edi. London: Academic Press; 1982.

[42] Lowell S, Shields JE, Thomas MA, Thommes M. Characterization of Porous Solids and Powders: Surface Area, Pore Size and Density. New York: Springer Science+Business Media; 2004. https://doi.org/10.1007/978-1-4020-2303-3.

[43] Thommes M, Kaneko K, Neimark A V., Olivier JP, Rodriguez-Reinoso F, Rouquerol J, et al. Physisorption of gases, with special reference to the evaluation of surface area and pore size distribution (IUPAC Technical Report). Pure Appl Chem 2015;87:1051–69. https://doi.org/10.1515/pac-2014-1117.

[44] Zhang Y, Barber TJ, Hu Q, Bleul M, El-Sobky HF. Complementary neutron scattering, mercury intrusion and SEM imaging approaches to micro- and nano-pore structure characterization of tight rocks: A case study of the Bakken shale. Int J Coal Geol 2019;212:103252.

[45] Washburn EW. Note on a Method of Determining the Distribution of Pore Sizes in a Porous Material. Proc Natl Acad Sci 1921;7:115–6. https://doi.org/10.1073/pnas.7.4.115.

[46] Ferreiro JP, Wilson M, Vázquez EV. Multifractal Description of Nitrogen Adsorption Isotherms. Vadose Zo J 2009;8:209–19. https://doi.org/10.2136/vzj2008.0007.

[47] Liu K, Ostadhassan M, Zou J, Gentzis T, Rezaee R, Bubach B, et al. Multifractal analysis of gas adsorption isotherms for pore structure characterization of the Bakken Shale. Fuel 2018;219:296–311.

[48] Wang Y, Cheng H, Hu Q, Liu L, Jia L, Gao S, et al. Pore structure heterogeneity of Wufeng-Longmaxi shale, Sichuan Basin, China: Evidence from gas physisorption and multifractal geometries. J Pet Sci Eng 2022;208:109313. https://doi.org/10.1016/J.PETROL.2021.109313.

[49] Buczkowski S, Hildgen P, Cartilier L. Measurements of fractal dimension by box-counting: a critical analysis of data scatter. Phys A Stat Mech Its Appl 1998;252:23–34. https://doi.org/10.1016/S0378-4371(97)00581-5.

[50] Halsey TC, Jensen MH, Kadanoff LP, Procaccia I, Shraiman BI. Fractal measures and their singularities: The characterization of strange sets. Nucl Phys B (Proceedings Suppl 1987;2:501–11. https://doi.org/10.1016/0920-5632(87)90036-3.

[51] Chhabra A, Jensen RV. Direct Determination of the f (c) Singularity. Spectrum 1989.

[52] Sing KSW, Everett DH, Haul RAW, Moscou L, Pierotti RA, Rouquerol J, et al. Reporting Physisorption Data for Gas/Solid Systems with Special Reference to the Determination of Surface Area and Porosity. Pure Appl Chem 1985;57:603–19. https://doi.org/10.1351/pac198557040603.

[53] Wu J, Fan T, Gomez-Rivas E, Gao Z, Yao S, Li W, et al. Impact of pore structure and fractal characteristics on the sealing capacity of Ordovician carbonate cap rock in the Tarim Basin. China Mar Pet Geol 2019;102:557–79.

[54] Ukaomah CF, Zhang L, Xu Y, Sun M, Yang B, Madaki AI, et al. Pore Structure and Seal Capacity of Ilaro Formation Shales in the Eastern Dahomey Basin: Implications from Mercury Injection Capillary Pressure and Spontaneous Imbibition Analyses. Energy Fuels 2021;35(12):10086–101.

[55] Guiltinan EJ, Espinoza DN, Cockrell LP, Cardenas MB. Textural and compositional controls on mudrock breakthrough pressure and permeability. Adv Water Resour 2018;121:162–72. https://doi.org/10.1016/J.ADVWATRES.2018.08.014.

[56] Medina CR, Mastalerz M, Lahann RW, Rupp JA. A novel multi-technique approach used in the petrophysical characterization of the Maquoketa Group (Ordovician) in the southeastern portion of the Illinois Basin: Implications for seal efficiency for the geologic sequestration of CO_2. Int J Greenh Gas Control 2020;93:102883. https://doi.org/10.1016/j.ijggc.2019.102883.

[57] Ma L, Fauchille AL, Ansari H, Chandler M, Ashby P, Taylor K, et al. Linking multi-scale 3D microstructure to potential enhanced natural gas recovery and subsurface CO_2 storage for Bowland shale. UK Energy Environ Sci 2021;14:4481–98. https://doi.org/10.1039/d0ee03651j.

[58] Dai X, Wang M, Wei C, Zhang J, Wang X, Zou M. Factors affecting shale microscopic pore structure variation during interaction with supercritical CO_2. J CO_2 Util 2020;38:194–211. https://doi.org/10.1016/J.JCOU.2020.01.021.

[59] Goodman A, Sanguinito S, Tkach M, Natesakhawat S, Kutchko B, Fazio J, et al. Investigating the role of water on CO_2-Utica Shale interactions for carbon storage and shale gas extraction activities – Evidence for pore scale alterations. Fuel 2019;242:744–55. https://doi.org/10.1016/j.fuel.2019.01.091.

[60] Curtis JB. Fracture and Shale Systems. Am Assoc Pet Geol Bull 2002;86:1921–38. https://doi.org/10.1016/b978-0-12-815563-9.00013-6.

[61] Zhang R, Liu S, Fan L, Blach TP, Sang G. Unraveling high-pressure gas storage mechanisms in shale nanopores through SANS. Environ Sci Nano 2021;8:2706–17. https://doi.org/10.1039/d1en00419k.

[62] Pei P, Ling K, He J, Liu Z. Shale gas reservoir treatment by a CO_2-based technology. J Nat Gas Sci Eng 2015;26:1595–606. https://doi.org/10.1016/j.jngse.2015.03.026.

[63] Sun M, Zhang L, Hu Q, Pan Z, Yu B, Sun L, et al. Multiscale connectivity characterization of marine shales in southern China by fluid intrusion, small-angle neutron scattering (SANS), and FIB-SEM. Mar Pet Geol 2020;112:104101. https://doi.org/10.1016/j.marpetgeo.2019.104101.

[64] Yong M, Zhejun P, Ningning Z, et al. Experimental study of anisotropic gas permeability and its relationship with fracture structure of Longmaxi Shales, Sichuan Basin, China. Fuel 2016;180:106–15. https://doi.org/10.1016/j.fuel.2016.04.029.

[65] Yuling T, Zhejun P, Xia-Ting F, et al. Laboratory characterisation of fracture compressibility for coal and shale gas reservoir rocks: A review. Int. J. Coal Geol. 2019;204:1–17. https://doi.org/10.1016/j.coal.2019.01.010.